Assessment of cloud properties from the reanalysis with satellite observations over East Asia

Bin Yao[1,2], Chao Liu[1,2], Yan Yin[1,2], Zhiquan Liu[3], Chunxiang Shi[4], Hironobu Iwabuchi[5], and Fuzhong Weng[6]

[1]Collaborative Innovation Center on Forecast and Evaluation of Meteorological Disasters, Nanjing University of Information Science & Technology, Nanjing 210044, China

[2]Key Laboratory for Aerosol-Cloud-Precipitation of China Meteorological Administration, School of Atmospheric Physics, Nanjing University of Information Science & Technology, Nanjing 210044, China

[3]National Center for Atmospheric Research, Boulder, CO 80301, USA

[4]National Meteorological Information Center, China Meteorological Administration (CMA), Beijing 100081, China

[5]Center for Atmospheric and Oceanic Studies, Graduate School of Science, Tohoku University, Sendai, Miyagi 980-8578, Japan

[6]Chinese Academy of Meteorological Sciences, Beijing 100081, China

Correspondence to: Chao Liu (chao_liu@nuist.edu.cn)

Abstract. Extensive observational and numerical investigations have been performed to better characterize cloud properties. However, due to the large variations of cloud spatiotemporal distributions and physical properties, quantitative depictions of clouds in different atmospheric reanalysis datasets are still highly uncertain, and cloud parameters in the models to produce the datasets remain largely unconstrained. A radiance-based evaluation approach is introduced and performed to assess the quality of cloud properties by directly comparing reanalysis-driven forward radiative transfer results with radiances from satellite observation. The newly developed China Meteorological Administration Reanalysis data (CRA), the ECMWF's Fifth-generation Reanalysis (ERA5), and the Modern-Era Retrospective Analysis for Applications, Version 2 (MERRA-2), which all provide sufficient diagnostic cloud information, are considered. To avoid the influence of assumptions and uncertainties on satellite retrieval algorithms and products, the radiative transfer model (RTM) is used as a bridge to "translate" the reanalysis to corresponding satellite observations. Then, the simulated reflectance and brightness temperatures (BTs) are directly compared with observations from the Advanced Himawari Imager (AHI) onboard the Himawari-8 satellite in the region from 80° E to 160° W between 60° N and 60° S, especially for results over East Asia. The analysis reveals that CRA better represents the total and mid-layer cloud cover than the other two reanalysis datasets. The simulated BTs for CRA and ERA5 are close to each other in many pixels, whereas the vertical distributions of cloud properties are significantly different, and ERA5 depicts a better deep convection structure than CRA reanalysis. Comparisons of the BT differences (BTDs) between the simulations and observations suggest that the water clouds are generally overestimated in ERA5 and MERRA-2, whereas the ice cloud is responsible for the overestimation over the center of cyclones in ERA5. Overall, the cloud from CRA, ERA5, and MERRA-2 show their own advantages in different aspects.

The ERA5 reanalysis is found to have the most capability in representing the cloudy atmosphere over East Asia, and the results in CRA are close to those in ERA5.

1 Introduction

As an important element in the Earth atmosphere, clouds play a vital role in the global radiation budget, water cycle, and climate change. Cloud formation is governed by the balance between dynamical, thermodynamic, and microphysical processes (Boucher et al., 2013). Although the representation of cloud in different atmospheric datasets and cloud evolution in regional and global numerical models have been significantly improved in the past few decades (Cess et al., 1989; Cotton et al, 2003; Arakawa, 2004), cloud is still one of the dominant uncertainties in the atmosphere, and causes difficulties in understanding the energy balance and climate change mechanisms (Dufresne and Bony, 2008; Boucher et al., 2013).

The atmospheric reanalysis, a dataset that combines observations and forecasting products (Dee et al., 2011), provides multivariate records of the global atmospheric circulation, and is widely used in the studies of climate change, cloud property retrieval, and the initialization of numerical modeling. With the advances in computation capability and the improvement of global observing systems, an increasing number of observed datasets are assimilated into the reanalysis by more advanced data assimilation methods and systems, and the reanalysis is being closer to realistic atmospheres. From the late period of the last century, a series of reanalysis data have been produced, for example, the National Centers for Environmental Prediction (NCEP) 40-yr Reanalysis Project (Kalnay et al., 1996), the 40-year ECMWF Reanalysis (ERA-40; Uppala et al., 2005), the Japanese 25-year Reanalysis (JRA-25; Onogi et al., 2007), the Modern-Era Retrospective Analysis for Research and Applications (MERRA; Rienecker et al., 2011), the ECMWF's Interim Reanalysis (ERA-Interim; Dee et al., 2011), and the Japanese 55-year Reanalysis (JRA-55; Kobayashi et al., 2015). Though some schemes and systems that support the assimilation of cloud-affected satellite radiance are developed (Chevallier et al., 2004; MaNally, 2009), clouds are difficult to be assimilated into the reanalysis, instead, they are forecasted by numerical weather prediction models (Free et at., 2016). Thus, although many atmospheric parameters in the reanalysis data are increasingly confident, the cloud is still challenging, and it is important yet difficult to accurately and reasonably assess the cloud properties in the reanalysis.

Because of large advantages of spatial coverages, observed atmosphere from satellite platforms is the best choice in the evaluation of output fields from numerical models. Some previous studies have conducted evaluations of reanalysis or model outputs based on satellite retrieved products. This is known as the satellite- or retrieval-based approach. Interesting results are achieved by this method (Jakob, 1999; Waliser et al., 2009; Hashino et al., 2013), especially for the long-term cloud cover in the reanalysis. However, some evaluations by the retrieval-based approach may be questionable (Matsui, et al., 2014) because of the inverse solving process in satellite retrieval. Many assumptions or parameters are needed to infer unknown quantities, and this will introduce some inevitable uncertainties. For example, although the vertical cloud profile is one of the most essential properties in most models, the single homogeneous layer cloud assumption is widely used in most satellite retrieval algorithms for cloud optical and microphysical properties (Wind et al., 2013; Yang et al., 2015), and the artificial

assumption will bring many uncertainties in cloud products. For example, the average relative differences of ice optical depth retrieved by Advanced Himawari Imager (AHI)/Himawari-8 and collocated Moderate Resolution Imaging Spectroradiometer (MODIS) are as large as 40% (Lai et al., 2019), and even MODIS products from different collections show significant differences (Yi et al., 2017a; 2017b). Moreover, the scattering properties of cloud particle model themselves are with lots uncertainties, and they are inconsistence in different retrieval approaches. Any mismatch in cloud optical parameterizations or retrieval algorithms could induce large bias in the retrieval and simulations (Yi et al., 2017a; 2017b).

The retrieval-based evaluation is still an indispensable approach in the evaluation of atmospheric properties from various simulations, and quantitative and qualitative analysis of the cloud optical properties (e.g., the cloud effective radius and optical depth) can be directly evaluated. However, to avoid uncertainties associated with satellite retrieval algorithms and platforms, an alternative radiance-based comparison is chosen for the cloud properties assessment in our study. In this approach, simulated radiative parameters, such as brightness temperature (BT) in the infrared (IR) channels or microwave channels and reflectance in the solar channels, can be calculated by a forward radiative transfer model (RTM), and the radiative variables can be directly compared with satellite radiative observations. The RTM helps us build a bridge between model atmospheric parameters (e.g., the reanalysis dataset) and direct satellite observations (Zhang et al., 2019). This will effectively avoid frustration from the uncertainties of satellite retrieval algorithms and products. This approach was first introduced to evaluate simulated cloud fields in the thermal IR channels by Morcrette (1991) and Yu et al. (1991). With the advantages of confident radiative information and the diversity of satellite channels, the radiance-based method has been applied to evaluate different cloud microphysics schemes (Han et al., 2013), precipitation microphysics schemes (Hashino et al., 2013), and even aerosol properties (Chaboureau et al., 2007), and became an important way to better understand the microphysical and radiative properties of clouds, precipitation, and other atmospheric parameters.

In this study, we extend the application of radiance-based approach to assess the cloud properties from three reanalysis datasets: the China Meteorological Administration Reanalysis (CRA), the ECMWF's Fifth-generation Reanalysis (ERA5; Hersbach and Dee, 2016) and the Modern-Era Retrospective Analysis for Research and Applications, Version 2 (MERRA-2; Gelaro et al., 2017). This is a new aspect to evaluate cloud and atmosphere properties from different atmospheric datasets. The radiative parameters (i.e., BTs in the IR channels and reflectance in the solar channels) from the Advanced Himawari Imager (AHI) onboard the Himawari-8 satellite (Bessho et al., 2016) are used as the observations.

This paper is organized as follows. The datasets are introduced in Section 2, and the coupled method between cloud microphysical parameters in the reanalysis and optical parameters that are supported by the RTMs are described in Section 3. A detailed radiance-based evaluation of cloud properties from the reanalysis, including a case assessment and a long-term comparison performed with a 36-day dataset (total of 144 realizations) spanning one year, is presented in Section 4. Section 5 summarizes the study.

2 Dataset

The newly developed Chinese first-generation atmospheric reanalysis, CRA, is based on the use of the National Oceanic and Atmospheric Administration (NOAA) Global Forecast System (GFS) model and Gridpoint Statistical Interpolation (GSI) 3DVAR data assimilation system (Wu et al., 2002; Kleist et al., 2009) with a T574 spectral resolution (34km grid spacing). The final CRA products will span the period from 1979 to present and is targeted to be produced and released in late 2020. An interim version of CRA (CRA-interim) for a 10-year period (1 January 2007 – 31 December 2016) at a 6-hourly time interval was produced in February 2018. An abundance data from in-situ observations and multiple satellite instruments, especially for the East Asian regions, have been assimilated into CRA-interim. More than 50 kinds of satellite observations, e.g., microwave radiance from TOVS, ATMS, and MWHS, infrared radiance from IASI and CrIS, ocean wind data from MetOp and SSM/I, and the atmospheric motion vector data from GOES, MTSAT, Himawari-8, MODIS, and AVHRR, are considered (Wang et al., 2018). Moreover, compared to the NCEP Climate Forecast System Reanalysis (CFSR), more Chinese surface and radiosonde datasets are assimilated into the CRA reanalysis (Liao et al., 2018). Those improvements significantly help to improve the capability of CRA in reproducing the realistic atmosphere. The CRA-interim data used in the study are in 47 pressure levels from the surface to 0.27 hPa with a horizontal resolution of 0.3125° × 0.3125°.

The ERA5 is the latest released numerical dataset of the recent climate. It is currently available for the period from 1979 to present at a 3-hourly time interval, and will be extended from 1950 to present. Satellite observed BTs from AMSRE, SSM/I, SSMIS, and TMI are assimilated for the cloud liquid water, column water vapour, and humidity sensitivities analysis, and BTs from GOES IMAGER, SEVIRI, MVIRI, and AHI are used for the analysis of water vapour and surface/cloud top temperature. All the aforementioned observations are assimilated into ERA5. The spatial resolution of the ERA5 dataset is 0.25° × 0.25°, and the atmospheric data are with 37 pressure levels from the surface to 1 hPa (Hersbach and Dee, 2016).

The MERRA-2 is the atmospheric reanalysis produced by the Global Modeling and Assimilation Office (GMAO) of the National Aeronautics and Space Administration (NASA), with the Goddard Earth Observing System (GEOS) atmospheric data assimilation system. It provides data from 1980 to present and is designed to build a bridge between the first MERRA reanalysis data and the project's long-term goal of developing an integrated Earth system analysis (IESA; Gelaro et al., 2017). Compared with MERRA reanalysis, microwave and infrared radiances from ATOVS and ATMS, hyperspectral infrared radiances from IASI and CrIS, and the geostationary radiances from MSG SEVIRI and the GOES-11, GOES-13, and GOES-15 satellites are considered. In this study, the data used from MERRA-2 is at a spatial resolution of 0.5° × 0.625° with 42 levels from the surface to 0.1 hPa.

To compare the quality of the three reanalysis datasets, satellite observed data from Himawari-8 are used. Launched on 7 October, 2014 and operated by the Japan Meteorological Agency (JMA) since 2015, the Himawari-8 is one of the new generation satellite members of the Multi-functional Transport Satellites (MTSATs; Da, 2015; Bessho et al., 2016). The AHI, which is a radiometer with 16 bands from the solar to IR range, is on board the Himawari-8 to observe the Earth from 80° E to 160° W between 60° N and 60° S. The spatial resolution of the observations is 0.5–2 km and the temporal resolution is 2.5–10 minutes (Iwabuchi et al., 2018). With high spatial and temporal sampling, the AHI measurement is valuable for disaster monitoring and cloud studies, especially for the region over East Asia.

For consistency in the comparison, all datasets used in this study are at a 6-hourly time interval, and the horizontal resolutions are re-gridded by the inverse distance weighted method to match the spatial distribution of the CRA (Guan and Wang, 2007; Holz et al., 2008). An 8-day case and a general comparison with a 36-day dataset (total of 144 realizations) spanning one year are chosen. Although the size of the evaluated datasets is small, the statistical results are credible, and the significant features are presented.

3 Methodology

With our focus on cloudy atmospheres, the accuracy of cloud properties is one of the most critical factors for the reliability of the evaluation. Cloud effective radius and optical depth are key microphysical and optical parameters in determining the radiation property in each atmospheric layer. However, variables from the reanalysis, e.g., cloud mixing ratio, cannot be directly supported by the fast RTM, and therefore cannot be directly compared with the satellite retrieved cloud optical properties. Thus, a reasonable coupled method between the microphysical properties in the reanalysis and the optical parameters that are comparable to satellite retrieved cloud properties and supported by the RTM is important and challenging. Table 1 lists the geophysical parameters in the reanalysis that are used in our study. A cloud coupled approach with less empirical or semi-empirical assumptions is performed. In each grid box, the occurrence of cloud or hydrometeor particles is diagnosed with cloud mixing ratio (q_c) larger than 0.001 g/kg and the relationship between relative humidity and cloud amount (Slingo, 1980). Ignoring little BT/reflectance bias caused by the mixed-phase cloud, a temperature threshold of 253 K is used to distinguish cloud phase. If the temperature of cloud layer is larger than 253 K, then the grid box is regarded as a water cloud, otherwise the grid box is regarded as an ice cloud (Mazin, 2004).

The effective radius (R_w) in each water cloud grid box is approximated by the cloud mixing ratio (q_c) and number concentration (N_w) (Thompson et al., 2004):

$$R_w = \frac{1}{2} \times \left(\frac{6\rho_a q_c}{\pi \rho_w N_w}\right)^{\frac{1}{3}} \quad (1)$$

where ρ_a is the density of air, which is determined by the pressure and temperature in the corresponding layer. The density of water cloud particles (ρ_w) is assumed to be 1000 kg/m^3. The water cloud number concentration of $N_w = 3 \times 10^8$ m^{-3} is assumed over the continent and $N_w = 1 \times 10^8$ m^{-3} is used over the ocean region (Miles et al., 2000).

The ice cloud effective radius (R_i) is obtained by the relationship between mass extinction coefficient (k) and cloud effective radius. The k can be given by an empirical relationship based on in-situ measurements (Heymsfield and McFarquhar, 1996; Platt, 1997; Heymsfield et al., 2003):

$$k = 0.018 \times (\mathrm{IWC})^{-0.14} \quad (2)$$

where IWC is the corresponding ice water content, and it is obtained from the cloud mixing ratio and density of air. Once k is produced, the corresponding R_i can be available from the cloud property database.

The optical depth determines the attenuation of radiation in the cloud layer. When the cloud effective radius (R_w *or* R_i) and the corresponding k are given, the cloud optical depth (τ) in the visible wavelength can be obtained by:

$$\tau = k \times \mathrm{CWP} \quad (3)$$

where CWP is the cloud (water or ice phase cloud) water path in each grid box and is found by integrating the cloud water content (CWC) from the cloud base (h_{base}) to top (h_{top}):

$$\mathrm{CWP} = \int_{h_{base}}^{h_{top}} \mathrm{CWC}\, dh \quad (4)$$

Then the cloud optical depth can be directly compared with the satellite retrieved cloud optical depth, and be converted into the corresponding optical depth at a specific wavelength when performing the RTM simulations.

It should be noted that schemes for both cloud optical properties (e.g., ice cloud model) in the RTM and coupling between atmospheric reanalysis and RTM (e.g., approximation of cloud effective radius) may influence simulated BTs/reflectances, although the influences are relatively minor compared to presences of clouds (cloud amount). The potential numerical uncertainties due to different schemes will be performed with more details in further studies.

4 Evaluation of the reanalysis

In the radiance-based evaluation, the Community RTM (CRTM) is used to calculate satellite observed radiative variables based on the synthetic atmospheric variables in the reanalysis. The CRTM is designed to simulate radiance and radiance gradients at the (TOA), and has been widely applied in radiance assimilation, remote sensing sensor calibration, climate reanalysis and so on. Procedures for solving the radiative transfer in the model are divided into various independent modules (e.g., gaseous absorption module, surface emissivity module, and cloud absorption/scattering module) (Chen et al., 2008; Ding et al., 2010). To improve the computational efficiency, the advanced fast adding-doubling method (ADA) method is used (Liu and Weng, 2006), and it is 1.7 times faster than the vector discrete ordinate method (Weng, 1992) and 61 times faster than the classical adding-doubling method (Twomey et al., 1966; Hansen and Hovenier, 1971). Four major surface types (i.e., water, land, ice, and snow) are included in the surface emissivity module, and the corresponding spectral library from visible to microwave wavelengths is pre-prepared for the emissivity calculation (Chen et al., 2008; Baldridge et al., 2009).

To minimize the numerical errors and uncertainties from radiative transfer computation, the cloud optical property look-up tables (LUTs) in the absorption/scattering module of CRTM are optimized before the simulation. We recalculate the single-scattering optical properties of water clouds by Lorenz-Mie theory (Mie, 1908). The single-scattering optical properties of ice clouds are from the data library developed by Yang et al. (2013), and we consider the ice cloud model based on aggregate columns with eight elements and severely roughened surface. A gamma size distribution with an effective variance of 0.1 (Hansen and Travis, 1974) is assumed to compute the bulk scattering properties (i.e., the extinction coefficient, single-scattering albedo, asymmetry factor and phase function coefficients). Validation of the CRTM with the new optical property LUTs is presented in Yao et al. (2018), and the BTDs between the CRTM and rigorous models in different channels are generally less than 1 K for ice clouds. For water clouds, the biases in the IR windows channels may reach to 2 K for optical

thin clouds and vary between -1 and 1 K in the water vapor channel. Moreover, compared to the default CRTM model, the update can substantially improve CRTM simulations on cloudy atmospheres (Yi et al., 2016; Yao et al., 2018).

To obtain the most realistic representation of the radiance from the TOA, the full layer atmospheric profiles (i.e., the pressure, temperature, and water vapor) and cloud optical properties that are computed in Section 3 are directly kept and adopted by the CRTM for the calculation of gas absorption and emission, and cloud scattering. The surface characteristics (e.g., surface type, altitude, and surface temperature) are also necessary for the CRTM to give the surface radiative property. Because the ozone absorption is insensitive in the channels of interest, the climatological ozone profiles are used in the simulation.

4.1 Case assessment

We first present a comparing typical case study to provide a detailed assessment of the cloud properties in three reanalysis datasets from 10 to 17 September 2016, the super typhoon Meranti, which is one of the most powerful tropical cyclones on record, was monitored. The extremely favorable atmospheric environment, including adequate water vapor, increased outflow in the upper layer, and unusually warm sea surface temperature, intensified the structure and energy of the typhoon. Meanwhile, on 11 September 2016, another tropical depression was detected and monitored over the Northwest Pacific Ocean, and it evolved into the typhoon Malakas on 13 September. The interaction of the two typhoons increased the water vapor transportation, which promoted the development of deeper and thicker clouds, and the rapid enhancement of the typhoons (Zhou and Gao, 2016). When Meranti passed over the Philippines and China, it produced heavy rain and hurricane-force winds and caused extensive damage. Note that even for this case study, we consider a period over eight days covering 32 time steps.

Figure 1 shows the spatial distribution patterns of the reflectance in the 0.64- and 1.6-μm channels. The observed and simulated results are taken at 00:00 UTC on 12 September 2016. Four typical regions marked by red boxes are chosen for better understanding and illustration. For these two channels, atmospheric profiles have little effect on the simulated reflectance, and the differences are mainly contributed by cloud properties. Because the channel in the visible wavelength (0.64-μm) is non-absorbing, the reflectance is primarily constrained by the cloud optical depth. Therefore, some cloud macro characteristics can be recognized from the result in this channel. The pixels with reflectance close to 1 (the whiter points) indicate the region covered by optically thick clouds. A qualitative comparison between the observation and the simulation shows that the results for CRA reanalysis more reasonably represent the cloud spatial distribution than those for the other two reanalysis datasets. The simulations from ERA5 and MERRA-2 obviously overestimate the cloud cover, and the overestimated cloud pixels are mostly over the ocean regions, for example, the region B, C and surrounding areas. In the 1.6-μm channel, the radiance observed from the TOA is significantly different for different phase clouds. Because ice particles have a stronger absorption property, the reflectance in this channel is usually smaller for pixels covered by ice clouds than those covered by water clouds. Thus, we can give a general distinction of the cloud phase based on the information in this shortwave IR channel. The similar characteristics between the observation and simulation over region A indicate that CRA,

ERA5, and MERRA-2 all have capabilities to distinguish ice and water phase clouds. Comparing the results over region B, the three reanalysis datasets all represent the cloud phase characteristics of the cyclones. More pixels with larger reflectance values for ERA5 suggest that although the cloud distributions in ERA5 and MERRA-2 are both overestimated over region B, the causes for the results are different. Some overestimated clouds in ERA5 reanalysis are from water phase clouds, whereas they are mostly caused by ice phase clouds in MERRA-2. For pixels over regions C and D, the overestimation comes from the water cloud in ERA5 and MERRA-2.

Different from the reflectance in the solar channels, the BTs in the IR channels are available for both daytime and nighttime. For further assessment and comparison, the discussion below is mostly based on the results in the three IR channels (one is in the water vapor channel, and two are in the window channels), and the time period is the same as that in Figure 1. Figure 2 illustrates the observed BTs in the 6.2-, 8.6-, and 11.2-μm channels, and the brightness temperature differences (BTDs) between the simulated BTs from CRA, ERA5, and MERRA-2 and the observations. Some typical regions and pixels are marked by boxes and dashed lines for better understanding and analysis. The IR window channels (8- to 12-μm) have less molecular absorption, and they are mostly sensitive to the surface temperature and cloud profiles. Therefore, the BTs in these channels are usually used to evaluate cloud properties or surface temperature (King et al., 1992; Mao et al., 2005). In the 6.2-μm channel, because of large sensitivity to a broad upper-layer humidity, the BTs are used to infer the mid- to high-layer water vapor content. Similar horizontal distributions between the observation and simulation in the two window channels generally confirm the dependable capabilities of the three reanalysis datasets to represent the atmospheric characteristics on cloudy and clear-sky. Over the entire region, the smallest average error of -1.59 K in the 11.2-μm channel indicates the best simulated BTs for ERA5, and the average results for CRA are close to it. However, the simulated error is much larger for MERRA-2, and the mean BTD is -9.19 K. Region A (i.e., the continental region) is characterized by low-layer clouds or clear-sky conditions, with a mean BT of 268.55, 270.12, 269.57, and 263.21 K for the observation, CRA, ERA5, and MERRA-2. The slightly underestimated cloud optical depth or cloud top height over this region may cause positive mean BTDs of 1.56 and 1.01 K for CRA and ERA5, respectively. However, the negative mean BTDs indicate that the properties are overestimated in the simulation for MERRA-2. Meanwhile, we need to note that some other atmospheric or surface properties may also cause similar results because of the uncertain and complex terrain features over the arid or semiarid regions. For the Tibetan Plateau, the limitation of the in-site observations results in uncertainties for the reanalysis datasets. Compared with the continental regions, larger simulation errors over ocean are primarily associated with more complex cloud distributions and structures. Over region B, broad simulated clouds with BTs between 220 and 250 K are largely responsible for the negative mean BTDs. The absolute BTD may reach as large as 80–90 K in the window channel, and it is almost 15–20 K larger than that over region A. More series excessive cloud pixels for MERRA-2 reanalysis explain the mean BTD of -19.02 K in the 11.2-μm channel. The negative mean BTDs over region B for CRA and MERRA-2 in the 6.2-μm channel suggest the excessive integrated mid- to high-layer water vapor content. The positive mean BTD for ERA5 over region B in this water vapor channel reveals a general insufficient water vapor content over the corresponding layer, and this results in the underestimation of upper-layer clouds. Meanwhile, the mean BTD of -2.35 K in the 11.2-μm channel indicates

that the overestimation of clouds should be related to low- or mid-layer clouds in this region. However, more water vapor content is represented in ERA5 over region C than in CRA and MERRA-2, and it is closer to the realistic atmosphere. Compared with the observation, a similar cyclone structure is captured in the imagery of IR window channel.

To give a quantitative evaluation of the results in Figure 1, the pixel-to-pixel comparisons over the entire region are shown in Figure 3. The color contours show the occurrence of the reflectance from the observations and simulations, and the color bar is shown on a logarithmic scale. The symmetry distribution with the high occurrence frequency following around the black 1:1 line for the results of CRA reveals a better agreement with the observed reflectance than the ERA5 and MERRA-2. The correlation coefficients of 0.66 and 0.62 for CRA in the 0.64- and 1.6-μm channels, respectively, reveal the best simulation in the solar channels. The simulations for ERA5 and MERRA-2 are clearly higher than the observations in some pixels, which yield a secondary high occurrence frequency band over the observed reflectance less than 0.2. This band corresponds to the overestimated cloud distributions in Figure 3. The correlation coefficients for ERA5 and MERRA-2 are 0.65 and 0.53, respectively, in the 0.64-μm channel, and they are less than 0.5 in the 1.6-μm channel. Figure 4 gives a similar pixel-to-pixel evaluation, but it is for the results in the IR channels. The correlation coefficients are all larger than 0.6, and the high occurrence is around the 1:1 line, revealing good agreements between the simulated and observed BTs in the 11.2-, 8.6-, and 6.2-μm channels, especially for CRA and ERA5.

To better illustrate the differences between cloudy and clear pixels, we distinguish them based on integrated column cloud optical depth in each pixel of 0.1 ($\tau > 0.1$ as cloudy pixels, and $\tau < 0.1$ as clear pixels), and Figure 5 shows the comparison between observed and simulated BTs in the 11-μm channel. The upper and lower panels are for cloudy and clear cases respectively. The upper panels show clearly wider distributions, which can also be indicated by smaller correlated coefficients, and this means that the cloud representation definitely introduces additional errors to the simulated BTs. Particularly for MERRA-2, much larger correlated coefficient for the clear pixels indicate that cloud property representation in MERRA-2 may significantly contribute to the differences from the observations.

To further demonstrate a quantitative evaluation of the results in the solar and IR channels, Figure 6 shows the probability (top panels) and cumulative probability (bottom panels) for the simulations and observations. The probability and cumulative probability are numerically calculated as:

$$Probability = \frac{Number\ of\ pixels\ with\ BT\ between\ BT_O - \Delta BT\ and\ BT_O + \Delta BT}{Total\ pixel\ number} \quad (5)$$

and:

$$Cumulative\ Probability = \frac{Number\ of\ pixels\ with\ BT\ less\ than\ BT_O}{Total\ pixel\ number} \quad (6)$$

In the IR window channels, the simulation from MERRA-2 overestimates the probability density against the observation between 220 and 275 K, generally reflecting the overestimation of mid- and mid-to-high layer cloud. For ERA5, the low-layer clouds are overestimated, but the high-layer clouds are underestimated, especially for clouds with a top temperature less than 230 K. Similar probability density structures between simulations for ERA5 and the observation in the 6.2-μm channel reveal a more reasonable water vapor distribution over the entire region, compared to those of the other two reanalysis datasets. Matsui et al. (2014) point out that the cumulative probability density is a better metric to assess the cloud

cover than satellite cloud products. If a threshold of BT approximately ~ 275 K in the 11.2-μm channel is assumed to be present of cloud pixels, the simulated cloud cover for CRA reanalysis achieves the best agreement with the observation. However, cumulative probability densities with BTs of ~ 275 K in ERA5 and MERRA-2 are larger than the corresponding value given by the observation, indicating an overestimation of cloud cover in the two datasets.

The atmospheric and cloud profiles (i.e., temperature, cloud effective radius and optical depth) over pixels of 18°N (marked by blue solid lines in Figure 2) are shown in Figure 7, and the corresponding integrated cloud mixing ratio, cloud optical depth and the number of cloud layers in each column are illustrated in Figure 8. Compared with the differences in the temperature profiles, the differences in the cloud profiles (cloud effective radius and optical depth) are more conspicuous among the three reanalysis. The vertical distribution of cloud property is insufficient over the low-to-mid layer in CRA, but in ERA5 reanalysis, the shortage is over the mid-to-high layer. On the one hand, in Figure 8, the integrated cloud properties cover up the inconsistency, and they are close to each other and result in similar simulated BTs in thin cloud pixels. On the other hand, similar integrated properties may cause significantly different BTs. Although the number of cloud layers and the integrated cloud optical depth are close in some pixels over region D (Figure 2), the simulated BTs in the 11.2-μm channel are much lower for CRA than for ERA5 reanalysis. This is caused by an abnormally excessive cloud mixing ratio or optical depth in the mid to high-layer. For MERRA-2 reanalysis, the widespread cloud mixing ratio brings in overestimated integrated cloud optical depth and cloud distributions in many pixels.

Different spectral channels have their own sensitivities to atmospheric and cloudy properties, so different cloud properties or atmospheric conditions can be detected and validated by the BTDs among different channels (Baum et al. 2000; Otkin, et al. 2009). Different from previous analysis based on single channel results, Figure 9 shows the observed and simulated BTDs of 11.2 – 12.4-μm, 8.6 – 11.2-μm, and 6.2 – 11.2-μm. The absorption of atmospheric water vapor in the 12.4-μm channel is greater than that in the 11.2-μm channel, and BTDs for 11.2 – 12.4-μm are usually positive in most regions. The cloud emissivity increases as the optical depth increases, which weakens the influence from the atmosphere below the cirrus clouds, and results in similar BTs in the two channels. Thus, smaller or zero BTDs are detected across the deep convective region (e.g., region C) and thick cloud regions. Meanwhile, because of the enhanced extinction of small ice particles in the 12.4-μm channel, the BTDs for thinner clouds around thick cloud pixels are large. Although the absorptive properties for different phase particles are similar in the 8.6-μm channel, the absorption for ice clouds is larger than that for water clouds in the 11.2-μm channel. Thus, the BTDs of 8.6 – 11.2-μm are positive for ice clouds and negative for water clouds in a typical case. Comparing the BTDs in the particular cloud region (e.g., region B), simulations for CRA are close to the observations, and the mean BTDs for them are 0.16 and 0.14 K, respectively. The negative mean BTDs in this region for ERA5 and MERRA-2 indicate the overestimation of water clouds or some underestimation of ice clouds. Because of the strong water vapor in the 6.2-μm channel and the negative temperature lapse rate in the troposphere, the BTDs of 6.2 – 11.2-μm are usually negative, and increase as the cloud height increases. The largest negative BTDs are often in the clear-sky region with sufficient water vapor and high surface temperature, and the positive or near zero BTDs correspond to overshooting cloud tops. Although the simulation for ERA5 reanalysis generally underestimates the mid to high-layer water vapor content and upper-layer cloud in

the entire and B region, as we mentioned before, if we isolate the overshooting cloud top by BTDs less than 0 K, the ERA5 has the closest structure and distribution to the observation over the three reanalysis datasets, corresponding to the analysis of region C.

To give a comprehensive evaluation of the cloud cover in the 8-day case, the BTD between 6.2- and 11.2-μm channels is used to classify pixels with clouds over different altitudes (Mecikalski and Bedka, 2006; Yao et al., 2018). Pixels with BTD between -45 and -30 K are understood as low-layer clouds, and the performance of the reanalysis for such clouds can be briefly demonstrated by:

$$Low\text{-}layer\ cloud\ ratio = \frac{Number\ of\ pixles\ with\ simulated\ BTD\ between -45\ and -30\ K}{Nummber\ of\ pixles\ with\ observed\ BTD\ between -45\ and -30\ K} \quad (7)$$

Similar, we have the mid-layer cloud ratio defined with BTDs between -30 and -10 K, and the high-layer cloud ratio given by pixel numbers with BTDs larger than -10 K. Ratios close to 1 indicate better performance of the cloud representation. The ratios as a function of time are illustrated in Figure 10. The CRA total cloud cover (TCC) ratio and mid-layer cloud ratio are mostly close to 1. The low-layer cloud ratio for MERRA-2 reanalysis is reasonable, but large mid- and high-layer cloud ratios (~ 1.6 and ~ 2) result in a substantial overestimation of TCC by approximately ~ 30%. For ERA5 reanalysis, the high-layer cloud ratio is approximately 0.7, and the low- and mid-layer cloud ratios are both larger than 1.

4.2 Long-term assessment

Further, a dataset spanning in 2016, with a total of 144 realizations (the realizations are from the 5th, 15th, and 25th of each month, and 4 snapshots in a 6-hourly time interval in each day are available) for each reanalysis is chosen to give a long-term assessment. Although the size of the dataset is not large enough, the significant characteristics are presented.

Figure 11 gives the ratio of clouds in different layers, and the definition and classification are the same as those in Figure 10, and the average values are listed in Table 2. For CRA and ERA5, the ratios of clouds show relatively weak variation over time, and the variation ranges and mean values are similar to the results in Figure 10. Clear seasonable variation is noticed for the bias of MERRA-2 cloud representation. Such seasonal variations are only shown for mid-layer clouds of ERA5, and are not shown for CRA. The simulated mid-, high-layer cloud ratios in MERRA-2 reanalysis in summer are significantly larger than those in other seasons. This is associated with the widespread overestimated cloud distributions, and the more frequent convective systems with thicker and higher clouds in summer aggravate the excessive overestimation.

Figure 12 illustrates the average BTDs between the simulations from CRA, ERA5, and MERRA-2 and the observations in the IR window and water vapor channels. Over the entire region, most pixels with average BTDs around 0 K in the IR window channels reveal a general good simulation from CRA and ERA5. Regions with larger deviations are generally over the arid or semiarid areas (as marked in region A in Figure 2), and the surrounding regions of the equator. For MERRA-2, the significant deviations with negative BTDs are over the Intertropical Convergence Zone (ITCZ), and the phenomenon is extended to the region around 20° N. Most pixels of positive BTDs in the water vapor channel for ERA5 indicate an underestimation of water vapor, and it is more obvious over the region of ITCZ.

Figure 13 shows the temporal variation of the mean BTDs (MBTD, i.e., average of the simulated and observed BT differences over the whole interested region), standard deviations of the BTDs (SBTD, i.e., corresponding standard deviation of the BTDs over the whole region), and correlation coefficient (R, correlation coefficient between simulated and observed BTs) in the 11.2-, 8.6-, and 6.2-μm channels, and the corresponding average values are listed in Table 2, together with the results for Figure 11. Three statistical parameters show seasonal variation characteristics over time and the largest errors are in summer because of more complex weather systems and clouds. The mean errors for the three reanalysis datasets are always negative in the IR window channels, demonstrating the general overestimation of clouds, especially for MERRA-2 in summer. In the 6.2-μm channel, the opposite phases of mean errors indicate the general underestimated mid to high-layer water vapor for ERA5 but an overestimation for CRA, corresponding to the analysis in Figure 12.

Overall, the spatial distributions of the average BTDs in Figure 11 and the statistical evaluation in Figure 13 indicate that the results for ERA5 have the best generalizable capability to represent atmospheric and cloud characteristics over the corresponding large region of the Himawari-8 observation, with the smallest absolute mean BTD of 0.92 K, the smallest standard deviation of BTDs of 12.77 K, and the largest correlation coefficient of 0.80. The results in CRA are close to those in ERA, whereas in MERRA-2, the deviations are slightly larger. Large and systemic deviations for the three reanalysis are mostly over the oceanic region around the equator and areas with complex surface features. The atmospheric and cloud characteristics are complex and volatile, and the in-situ observations are limited over these regions. The atmospheric and cloud in the reanalysis are with lots of uncertainties.

5 Summary

This study performs an assessment of cloud properties from three reanalysis datasets (i.e., the CRA, ERA5, and MERRA-2) with the Himawari-8 satellite observation by a radiance-based approach. The atmospheric and cloud variables in the reanalysis are converted into BTs or reflectance, with the help of a reasonable cloud and atmosphere coupled method and the widely used forward RTM (i.e., CRTM), and they are compared and analysed with the satellite direct observations.

The assessment indicates that the atmospheric and cloud characteristics from CRA, ERA5, and MERRA-2 are mostly depicted. The BTs in the IR window channels (i.e., 11.2- and 8.6-μm) and reflectance in the 0.64-μm channel reveal the excellent TCC and mid-layer in CRA. For the results in MERRA-2, the low-layer clouds are more reasonable than clouds over other layers, and the widespread overestimated TCC is mostly caused by the overestimation of mid- and high-layer clouds. From the results in the 6.2-μm channel, obvious overestimated mid to high-layer water vapor is shown in CRA and MERRA-2, whereas it is underestimated in ERA5 over most regions. The BTD comparisons of 6.2 – 11.2-μm further suggest that ERA5 has the most reasonable overshooting cloud top structures and distributions. The reflectance in the 1.6-μm channel and the BTDs of 8.6 – 11.2-μm reflect the overestimated water vapor pixels over the ocean region in ERA5 and MERRA-2. However, it is slightly different over the center of the cyclone because more ice cloud pixels are depicted in ERA5 reanalysis.

Generally, the CRA, ERA5, and MERRA-2 are all capable of representing the atmospheric and cloud characteristics over the Himawari-8 observed region. Seasonal variation features over time are shown in a long-time assessment. The larger statistical errors occur over the oceanic region around the equator and areas with complex surface features, because of the complex atmospheric and cloud structures, and the limitation of in-site observations that can be assimilated into the reanalysis. The largest correlation coefficients of 0.80 and 0.90 between the simulations and observations in the IR window and water vapor channels, respectively, demonstrating that the ERA5 reanalysis achieves the generally best simulations. The results for CRA also reveal reasonable simulations, and they are close to those in ERA5, whereas for MERRA-2 reanalysis, the deviations are slightly larger. It should be noticed that both ERA5 and CRA reanalysis consider the Himawari-8 observations for assimilation (see Section 2), whereas the MERRA-2 does not. This may be one of the reasons that MERRA-2 has relatively poor performance on cloud representation in the Asia region.

Compared with the assessment by satellite retrieved cloud products, the feasible direct comparison of radiative parameters provides a more reasonable evaluation of the microphysical and radiative properties of the atmospheric and cloud properties from the reanalysis. It effectively avoids many uncertainties associated with satellite retrieved products, such as the scattering properties of cloud model, retrieval algorithms, and platforms, and more interesting results and information are obtained. Although the discussion in this manuscript is focus on the observed region of Himawari-8 satellite on cloudy atmosphere, this approach can be applied to perform the evaluation of more parameters (e.g., cloud, aerosol, precipitation, and so on) from different atmospheric datasets or modeled results. The radiance-based approach is a reasonable choice for the evaluation to avoid uncertainties due to retrieval products, and its drawbacks may be investigated in further studies. For, examples, differences between simulated and observed radiances can be contributed by both cloud and atmospheric variables, and these may be distinguished by considering the same atmospheric profiles in the RTM simulation. We believe more reasonable and qualitative analysis and interested information should be investigated and detected in the future, and it should have a chance to contribute to the improvement of cloud properties in regional or global models and the designation of observations.

Data availability.

The data in this study are available at: https://github.com/carrolyb/Reanalysis_Evaluation_2019/.

Author Contributions.

BY and CL designed the study, carried out the research, and performed data analysis. BY, CL, YY, ZL, CS, HI, and FW discussed the results and wrote the paper. All authors gave approval for the final version of the paper.

Competing interests.

The authors declare that they have no conflict of interest.

Acknowledgements.

We acknowledge funding supported by the Special Fund for Meteorological Scientific Research in Public Interest (GYHY 201506002), the National Natural Science Foundation of China (NSFS, grants 41975025 and 41590873), and the Postgraduate Research & Practice Innovation Program of Jiangsu Province (KYCX18_1004). The computation is supported by the National Supercomputer Center in Guangzhou (NSCC-GZ).

References

Arakawa, A.: The cumulus parameterization problem: Past, present, and future, J. Climate, 17, 2493-2525, https://doi.org/10.1175/1520-0442(2004)017<2493:RATCPP>2.0.CO;2, 2004.

Baldridge, A. M., Hook, S. J., Grove, C. I., and Rivera, G.: The ASTER spectral library version 2.0. Remote Sens. Environ., 113, 711-715, https://doi.org/10.1016/j.rse.2008.11.007, 2009.

Baum, B. A., Kratz, D. P., Yang, P., Ou, S. C., Hu, H., Soulen, P. F., and Tsay, S.-C.: Remote sensing of cloud properties using MODIS airborne simulator imagery during SUCCESS.I. Data and models, J. Geophys. Res., 105, 767-780, https://doi.org/10.1029/1999JD901089, 2000.

Bessho, K., Date, K., Hayashi, M., Ikeda, A., Imai, T., Inoue, H., Kumagai, Y., Miyakawa, T., Murata, H., Ohno, T., Okuyama, A., Oyama, R., Sasaki, Y., Shimazu, Y., Shimoji, K., Sumida, Y., Suzuki, M., Taniguchi, H., Tsuchiyama, H., Uesawa, D., Yokota, H., and Yoshida, R.: An Introduction to Himawari-8/9 – Japan's New-Generation Geostationary Meteorological Satellite, J. Meteor. Soc. Jpn., 94, 151-183, https://doi.org/10.2151/jmsj.2016-009, 2016.

Boucher, O., Randall, D., Artaxo, P., Bretherton, C., Feingold, G., Forster, P., Kerminen, V.-M., Kondo, Y., Liao, H., Lohmann, U., Rasch, P., Satheesh, S., Sherwood, S., Stevens, B., and Zhang, X.: Clouds and Aerosols, book section 7, p. 571-658, Cambridge Univ. Press, Cambridge, UK and New York, https://doi.org/10.1017/CBO9781107415324.016, 2013.

Cess, R. D., Potter, G. L., Blanchet, J. P., Boer, G. J., Ghan, S. J., Kiehl, J. T., Treut, H. LE., Li, Z.-X., Liang, X.-Z., Mitchell, J. F. B., Morcrette, J.-J., Randall, D. A., Riches, M. R., Roeckner, E. R., Schles, U., Slingo, A., Taylor, K. E., Washington, W. W., Wetherald, R. T., and Yagai, I.: Interpretation of cloud-climate feedbacks as produced by 14 atmospheric general circulation model, Science, 245, 513-516, https://doi.org/10.1126/science.245.4917.513, 1989.

Chaboureau, J.-P., Tulet, P., and Mari, C.: Diurnal cycle of dust and cirrus over West Africa as seen from Meteosat Second Generation satellite and a regional forecast model, Geophys. Res. Lett., 34, LO2822, https://doi.org/10.1029/2006GL027771, 2007.

Chen, Y., Weng, F., Han, Y., and Liu, Q.: Validation of the community radiative transfer model by using CloudSat data, J. Geophys. Res., 113, D00A03, https://doi.org/10.1029/2007JD009561, 2008.

Chevallier, F., Lopez, P., Tompkins, A. M., Janiskova´, M., and Moreau, E.: The capability of 4D-Var systems to assimilate cloud-affected satellite infrared radiances, Q. J.. R. Meteorol. Soc. 130, 917-932, https://doi.org/10.1256/qj.03.113, 2004.

Cotton, W. R., Pielke, R. A. Sr., Walko, R. L., Liston, G. E., Tremback, C. J., Jiang, H., McAnelly, R. L., Harrington, J. Y., Nicholls, M. E., Carrio, G. G., and McFadden, J. P.: RAMS 2001: Current status and future directions, Meteor. Atmos. Phys., 82, 5-29, https://doi.org/10.1007/s00703-001-0584-9, 2003.

Da, C.: Preliminary assessment of the Advanced Himawari Imager (AHI) measurement onboard Himawari-8 geostationary satellite, Remote Sens. Lett., 6, 637-646, https://doi.org/10.1080/2150704X.2015.1066522, 2015.

Dee, D. P., Uppala, S. M., Simmons, A. J., Berrisford, P., Poli, P., Kobayashi, S., Andrae, U., Balmaseda, M. A., Balsamo, G., Bauer, P., Bechtold, P., Beljaars, A. C. M., van de Berg, L., Kållberg, P., Kållber, M., Matricardi, M., McNally, A. P., Monge-Sanz, B. M., Morcrette, J.-J., Park, B.-K., Peubey, C., de Rosnay, P., Tavolato, C., Thépaut, J.-N., and Vitart, F.: The ERA-Interim reanalysis: configuration and performance of the data assimilation system, Q. J. Roy. Metero. Soc., 127, 553-597, https://doi.org/10.1002/qj.828, 2011.

Ding, S., Yang, P., Weng, F., Liu, Q., Han, Y., van Delst, P., Li, J., and Baum, B.: Validation of the community radiative transfer model, J. Quant. Spectrosc. Radiat. Transf., 112, 1050-1064, https://doi.org/10.1016/j.jqsrt.2010.11.009, 2010.

Dufresne, J.-L., and Bony, S.: An assessment of the primary sources of spread of global warming estimates from coupled atmosphere-ocean model, J. Climate, 21, 5135-5144, https://doi.org/10.1175/2008JCLI2239.1, 2008.

Free, M., Sun, B., and Yoo, H. L.: Comparison between Total Cloud Cover in Four Reanalysis Products and Cloud Measured by Visual Observations at US Weather Stations, J. Climate, 29, 2015-2021, https://doi.org/10.1175/JCLI-D-15-0637.1, 2016.

Gelaro, R., McCarty, W., Suárez, M. J., Todling, R., Molod, A., Takacs, L., Randles, C. A., Bosilovich, M. G., Reichle, R., Wargan, K., Copy, L., Cullather, R., Draper, C., Akella, S., Buchard, V., Conaty,, A., da Silve, A. M., Gu, W., Kim, G.-K., Koster, R., Lucchesi, R., Merkova, D., Nielsen, J. E., Partyka, G., Pawson, S., Putman, W., Rienecker, M., Schubert, S. D., Sienkiewicz, M., and Zhao, B.: The modern-era retrospective analysis for research and applications, version 2 (MERRA-2), J. Climate, 30, 5419-5454, https://doi.org/10.1175/JCLI-D-16-0758.1, 2017.

Guan, L. and Wang, Z.: Objective determination of AIRS cloud mask using co-located MODIS cloud mask, Scientia Meteorological Sincia, 27, 516-521, 2007.

Han, M., Braun, S. A., Matsui, T., and Williams, C. R.: Evaluation of cloud microphysics schemes in simulations of a winter storm using radar and radiometer measurements, J. Geophys. Res., 118, 1401-1419, https://doi.org/10.1002/jgrd.50115, 2013.

Hansen, J. E. and Hovenier, J. W.: The doubling method applied to multiple scattering of polarized light, J. Quant. Spectrosc. Radiat. Transf., 11, 809-812, https://doi.org/10.1016/0022-4073(71)90057-4, 1971.

Hansen, J. E. and Travis, L. D.: Light scattering in planetary atmospheres, Space. Sci. Rev., 16, 527-610, https://doi.org/10.1007/BF00168069, 1974.

Hashino, T., Satoh, M., Hagihara, Y., Kubota, T., Matsui, T., Nasuno, T., and Okamoto, H.: Evaluating cloud microphysics from NICAM against CloudSat and CALIPSO, J. Geophys. Res., 118, 7273-7292, https://doi.org/10.1002/jgrd.50564, 2013.

Hersbach, H. and Dee, D.: "ERA5 reanalysis is in production", ECMWF Nesletter, number 147, Spring 2016, p. 7, 2016.

Heymsfield, A. J., Matrosov, J. S., and Baum, B.: Ice water path optical depth relationships for cirrus and deep stratiform ice cloud layers, J. Appl. Meteor., 42, 1369-1390, https://doi.org/10.1175/1520-0450(2003)042<1369:IWPDRF>2.0.CO;2, 2003.

Heymsfield, A. J. and McFarquhar, G. M.: On the high albedos of anvil cirrus in the tropical Pacific warm pool: Microphysical interpretations from CEPEX and from Kwajalein, Marshall Islands, J. Atmos. Sci., 53, 2424-2451, https://doi.org/10.1175/1520-0469(1996)053<2424:HAOCIT>2.0.CO;2, 1996.

Holz, R. E., Ackerman, A., Nagle, F. W., Frey, R., Dutcher, S., Kuehn, R. E., Vaughan, M. A., and Baum, B.: Global Moderate Resolution Imaging Spectroradiometer (MODIS) cloud detection and height evaluation using CALIOP, J. Geophys. Res., 113, D00A19, https://doi.org/10.1029/2008JD009837, 2008.

Iwabuchi, H., Putri, N. S., Saito, M., Tokoro, Y., Sekiguchi, M., Yang, P., and Baum, B. A.: Cloud Property Retrieval from Multiband Infrared Measurements by Himawari-8, J. Meteor. Soc. Jpn., 96, 27-42, https://doi.org/jmsj.2018-001, 2018.

Jakob, C.: Cloud Cover in the ECMWF Reanalysis, J. Climate, 12, 947-959, https://doi.org/10.1175/1520-0442(1999)012<0947:CCITER>2.0.CO;2, 1999.

Kalnay, E., Kanamitsu, M., Kistler, R., Collins, W., Deaven, D., Gandin, L., Iredell, M., Saha, S., White, G., Woolen, J., Zhu, Y., Chlliah, M,, Ebisuzaki, W., Higgins, W., Janowiak, J., Mo, K. C., Ropelewski, C., Wang, J., Leetmaa, A., Reynolds, R., Jenne, R., and Joseph, D.: The NCEP/NCAR 40-Year Reanalysis Project, Bull. Amer. Meteorol. Soc., 77, 1757-1774, https://doi.org/10.1175/1520-0477(1996)077<0437:TNYRP>2.0.CO;2, 1996.

King, M. D., Kaufman, Y. J., Menzel, W. P., and Tanre, D.: Remote sensing of cloud, aerosol, and water vapor properties from the Moderate Resoluting Imaing Spectrometer (MODIS), IEEE Trans. Geosci, Remote Sens., 301, 2-27, https://doi.org/10.1109/36.124212, 1992.

Kleist, D. T., Parrish, D. F., Derber, J. C., Treadon, R., Wu, W.-S., and Lord, S.: Introduction of the GSI into the NCEP Global Data Assimilation System, Wea. Forecasting, 24, 1691-1705, https://doi.org/10.1175/2009WAF2222201.1, 2009.

Kobayashi, S., Ota, Y., Harada, Y., Ebita, A., Moriya, M., Onoda, H., Onogi, K., Kamahori, H., Kobayashi, C., Endo, H., Miyaoka, K., and Takahashi, K.: The JRA-55 Reanalysis: General specifications and basic characteristics, J. Meteor. Soc. Jpn. Ser., 93, 5-48, https://doi.org/10.2151/jmsj.2015-001, 2015.

Lai, R., Teng, S., Yi, B., Letu, H., Min, M., Tang, S., and Liu, C.: Comparison of Cloud Properties from Himawari-8 and Fengyun-4A Geostationary Satellite Radiometers with MODIS Cloud Retrievals, Remote Sens., 11, 1703, https://doi.org/10.3390/rs11141703, 2019.

Liao, J., Hu, K., Jiang, H., Cao, J., Jiang, L., Li, Q., Zhou, Z., Liu, Z., Zhang, T., and Wang, H.: Pre-Process and Data Selection for Assimilation of Conventional Observations in the CMA Global Atmospheric Reanalysis, Advances in Met S&T., 8, 133-142, https://doi.org/10.2969/j.issn.2095-1973.2017.01.018, 2018.

Liu, Q., and Weng, F.: Advanced doubling-adding method for radiative transfer in planetary atmosphere, J. Atmos. Sci., 63, 3459-3465, https://doi.org/10.1175/JAS3803.1, 2006.

Mecikalski, J. R. and Bedka, K. M.: Forecasting convective initiation by monitoring the evolution of moving cumulus in daytime GOES imagery, Mon. Wea. Rev., 134, 49-78, https://doi.org/10.1175/MWR3062.1, 2006.

Mao, K., Qin, Z., Shi, J., and Gong, P.: A practical split-window algorithm for retrieving land-surface temperature from MODIS data, Int. J. Remote Sens., 26, 3181-3204, https://doi.org/10.1029/2006GL026547, 2005.

Matsui, T., Santanello, J., Shi, J. J., Tao, W.-K., Wu, D., Peters-Lidard, C., Kemp, E., Chin, M., Starr, D., Sekiguchi, M., and Aires, F.: Introducing multisensory satellite radiance-based evaluation for regional Earth System modeling, J. Geophys. Res., 119, 8450-8475, https://doi.org/10.1002/2013JD021424, 2014.

Mazin, I. P.: Cloud Phase Structure: Experimental Data Analysis and Parameterization, J. Atmos. Sci., 63, 667-681, https://doi.org/10.1175/JAS3660.1, 2004.

McNally, A. P.: The direct assimilation of cloud-affected satellite infrared radiances in the ECMWF 4D-Var, Q. J. R. Meteorol. Soc. 135, 1214-1229, https://doi.org/10.1002/qj.426, 2009.

Mie, G.: Beiträge zur optic trüber medien, speziell kolloidaler metallösungen, Ann. Phys., 330, 337-445, 1908.

Miles, N. L., Verlinde, J., and Clothiaux, E. E.: Cloud Droplet Size Distributions in Low-Level Stratiform Clouds, J. Atmos. Sci., 57, 295-311, https://doi.org/10.1175/1520-0469(2000)057<0295:CDSDIL>2.0.CO;2, 2000.

Morcrette, J.-J.: Evaluation of model-generated cloudiness: Satellite-observed and model-generated diurnal variability of brightness temperature, Mon. Wea. Rev., 119, 1205-1224, https://doi.org/10.1175/1520-0493(1991)119%3C1205:EOMGCS%3E2.0.CO;2, 1991.

Onogi, K., Tsutsui, J., Koide, H., Sakamoto, M., Kobayashi, S., Hatsushika, H., Matsumoto, T., Yamazaki, N., Kamahori, H., Takahashi, K., Kadokura, S., WADA, K., Kato, K., Oyama, R., Ose, T., Mannoji, N., and Taira, R.: The JRA-25 Reanalysis, J. Meteor. Soc. Jpn, 85, 369-432, https://doi.org/10.2151/jmsj.85.369, 2007.

Otkin, J. A., Greenwald, T. J., Sieglaff, J., and Huang, H.-L.: Validation of a large-scale simulated brightness temperature dataset using SEVIRI satellite observations, J. Climate, 25, 4975-4992, https://doi.org/10.1175/2009JAMC2142.1, 2009.

Platt, C. M. R.: A Parameterization of the Visible Extinction Coefficient of Ice Clouds in Terms of the Ice/Water Content, J. Atmos. Sci., 54, 2083-2098, https://doi.org/10.1175/1520-0469(1997)054<2083:APOTVE>2.0.CO;2, 1997.

Rienecker, M. M., Suarez, M. J., Gelaro, R., Todling, R., Bacmeister, J., Liu, E., Bosilovich, M. G., Schubert, S. D., Takacs, L., Kim, G.-K., Bloom, S., Chen, J., Collins, D., Conaty, A., da Silva, A., Gu, W., Joiner, J., Koster, R. D., Lucchesi, R., Molod, A., Owens, T., Pawson, S., Pegion, P., Redder, C. R., Reichle, R., Robertson, F, R., Ruddick, A. G., Sienkiewicz, M., and Woollen, J.: MERRA: NASA's Modern-Era Retrospective Analysis for Research and Applications, J. Climate, 24, 3624-3648, https://doi.org/10.1175/JCLI-D-11-00015.1, 2011.

Slingo, J. M.: A cloud parameterization scheme derived from GATE data for use with a numerical model, Q. J. R. Meteorol. Soc., 106, 747-770, https://10.1002/qj.49710645008, 1980.

Thompson, G., Rasmussen, R. M., and Manning, K.: Explicit forecasts of winter precipitation using an improved bulk microphysics scheme, Part I: Description and sensitivity analysis, Mon. Wea. Rev., 132, 519-542, https://doi.org/10.1175/1520-0493(2004)132%3C0519:EFOWPU%3E2.0.CO;2, 2004.

Twomey, S., Jacobowitz, H., and Howell, H. B.: Matrix methods for multiple-scattering problems, J. Atmos. Sci., 23, 289-298, https://doi.org/10.1175/1520-0469(1966)023%3C0289:MMFMSP%3E2.0.CO;2, 1966.

Uppala, S. M., KÅllberg, P. W., Simmons, A. J., Andrae, U., da costa Bechtold, V., Fiorino, M., Gibson, J. K., Haseler, J., Hernandez, A., Kelly, G. A., Li, X., Onogi, K., Saarinen, S., Sokka, N., Allan, R. P., Andersson, E., Arpe, K., Balmaseda, M. A., Beljaars, A. C. M, van de Berg, L., Bidlot, J., Bormann, N., Caires, S., Chevallier, F., Dethof, A., Dragosavac, M., Fisher, M., Fuentes, M., Hagemann, S., Hólm, E., Hoskins, B. J., Isaksen, L., Janssen, P. A. E. M., Jenne, R., Mcnally, A. P., Mahfouf, J.-F., Morcrette, J.-J., Rayner, N. A., Saunders, R. W., Simon, P., Sterl, A., Trenberth, K. E., Untch, A., Vasiljevic, D., Viterbo, P., and Woollen, J.: The ERA-40 re-analysis, Q. J. R. Meteorol. Soc., 131, 2961-3012, https://doi.org/10.1256/qj.04.176, 2005.

Wang, M., Yao, S., Jiang, L., Liu, Z., Shi, C., Hu, K., Zhang, T., Zhang, Z., and Liu, J.: Collection and Pre-Processing of Satellite Remote-Sensing Data in CRA-40 (CMA's Global Atmospheric ReAnalysis), Advances in Met S&T., 8, 158-163, https://doi.org/10.3969/j.issn.2095-1973.2018.01.021, 2018.

Waliser, D. E., Li, J.-L. F., Woods, C. P., Austin, R. T., Bacmeister, J., Chern, J., Genio, A. D., Jiang, J. H., Kuang, Z., Meng, H., Minnis, P., Platnick, S., Rossow, W. B., Stephens, G. L., Sun-Mack, S., Tao, W.-K., Tompkins, A. M., Vane, D. G., Walker, C., and Wu, D.: Cloud ice: A climate model challenge with signs and expectations of progress, J. Geophys. Res., 114, D00A21, https://doi.org/10.1029/2008JD010015, 2009.

Weng, F.: A multi-layer discrete-ordinate method for vector radiative transfer in a vertically-inhomogeneous, emitting and scattering atmosphere: Theory. J. Quant. Spectrosc. Radiat. Transf., 47, 19-33, https://doi.org/10.1016/0022-4073(92)90076-G, 1992.

Wind, G., Da Silva, A. M., Norris, P. M., and Platnick, S.: Multi-sensor cloud retrieval simulator and remote sensing from model parameters-Part 1: Synthetic sensor radiance formulation, Geosci. Model Dev., 6, 2049-2062, https://doi.org/10.5194/gmd-6-2049-2013, 2013.

Wu, W. S., Purser, R. J., and Parrish, D. F.: Three-dimensional variation analysis with spatially inhomogeneous covariances, Mon. Wea. Rev., 130, 2905-2916, https://doi.org/10.1175/1520-0492(2002)130<2905:TDVAWS>2.0.CO;2, 2002.

Yang, P., Bi, L., Baum, B. A., Liou, K.-N., Kattawar, G. W., Mishchenko, M. I., and Cole, B.: Spectrally consistent scattering, absorption, and polarization properties of atmospheric ice crystals at wavelengths from 0.2 to 100 μm, J. Atmos. Sci., 70, 330-347, https://doi.org/10.1175/JAS-D-12-039.1, 2013.

Yang, P., Liou, K.-N., Bi, L., Liu, C., Yi, B., and Baum, B. A.: On the radiative properties of ice clouds: Light scattering, remote sensing, and radiation parameterization. Adv. Atmos. Sci., 32, 32-63, https://doi.org/10.1007/s00376-014-0011-z, 2015.

Yao, B., Liu, C., Yin, Y., Zhang, P., Min, M., and Han, W.: Radiance-based evaluation of WRF cloud properties over East Asia: Direct comparison with FY-2E observations, J. Geophys. Res., 123, 4613-4629, https://doi.org/10.1029/2017JD027600, 2018.

Yi, B., Yang, P., Liu, Q., van Delst, P., Boukabara, S.-A., and Weng, F.: Improvements on the ice cloud modeling capabilities of the Community Radiative Transfer Model, J. Geophys. Res., 121, 577-590, https://doi.org/10.1002/2016JD025207, 2016.

Yi, B., Rapp, A. D., Yang, P., Baum, B. A., and King, M. D.: A comparison of Aqua MODIS ice and liquid water cloud physical and optical properties between collection 6 and collection 5.1: Pixel-to-pixel comparisons, J. Geophys. Res., 122, 4528-4549, https://doi.org/10.1002/2016JD025586, 2017a.

Yi, B., Rapp, A. D., Yang, P., Baum, B. A., and King, M. D.: A comparison of Aqua MODIS ice and liquid water cloud physical and optical properties between collection 6 and collection 5.1: Cloud radiative effects, J. Geophys. Res., 122, 4550-4565, https://doi.org/10.1002/2016JD25654, 2017b.

Yu, W., Sèze, G., Treut, H. L., and Desbois, M.: Comparison of radiance fields observed by satellite and simulated by the LMD general circulation model. Dyn. Atmos. Oceans., 16, 147-165, https://doi.org/10.1016/0377-0265(91)90018-B, 1991.

Zhang, P., Lu, Q., Hu, X., Gu, S., Yang, L., Min, M., Chen, L., Xu, N., Sun, L., Bai, W., Ma, G., and Xian, D.: Latest progress of the Chinese Meteorological Satellite program and core data processing technologies, Adv. Atmos. Sci., 36, 1027-1045, 2019.

Zhou, G. and Gao, S.: Analysis of the September 2016 Atmospheric Circulation and Weather, Meteor. Mon., 42, 1560-1566, https://doi.org/10.7519/j.issn.1000-0526.2016.12.015, 2016.

610 **Table 1.** Geophysical parameters from the reanalysis datasets used in the assessment.

Ordinal	Parameters
1	Temperature at surface
2	Pressure at surface
3	Cloud mixing ratio
4	Atmospheric profiles (pressure, specific humidity, temperature, height)

Table 2. Average ratios of cloud pixels for different layer clouds in Figure 11, and the average values of the mean BTDs (MBTD), standard deviation of BTDs (SBTD), and correlation coefficient (R) between the observations and simulations in Figure 13.

Cloud	All			Spring			Summer			Autumn			Winter		
	CRA	ERA5	MERRA-2	CRA	ERA5	MERRA-2	CRA	ERA5	MERRA-2	CRA	ERA5	MERRA-2	CRA	ERA5	MERRA-2
Total	0.99	1.14	1.27	1.00	1.15	1.29	0.99	1.16	1.32	0.98	1.14	1.25	1.01	1.12	1.22
Low	0.87	1.15	1.04	0.86	1.17	1.07	0.85	1.14	0.99	0.87	1.14	1.00	0.90	1.15	1.10
Mid	1.03	1.28	1.45	1.06	1.27	1.48	1.06	1.37	1.58	0.99	1.29	1.42	1.01	1.20	1.31
High	1.45	0.69	1.76	1.50	0.69	1.80	1.41	0.70	2.03	1.46	0.67	1.80	1.44	0.68	1.43

11.2-μm	All			Spring			Summer			Autumn			Winter		
	CRA	ERA5	MERRA-2	CRA	ERA5	MERRA-2	CRA	ERA5	MERRA-2	CRA	ERA5	MERRA-2	CRA	ERA5	MERRA-2
MBTD	-2.08	-0.92	-7.45	2.53	-0.89	-7.53	-2.08	-1.29	-9.58	-1.84	-0.94	-7.43	-2.07	-0.56	-5.26
SBTD	15.66	12.77	17.53	15.53	12.69	17.29	16.39	13.42	19.24	14.83	12.84	17.35	14.92	12.14	16.24
R	0.75	0.80	0.65	0.75	0.80	0.66	0.72	0.78	0.59	0.74	0.80	0.66	0.77	0.83	0.70

8.6-μm	All			Spring			Summer			Autumn			Winter		
	CRA	ERA5	MERRA-2	CRA	ERA5	MERRA-2	CRA	ERA5	MERRA-2	CRA	ERA5	MERRA-2	CRA	ERA5	MERRA-2
MBTD	-2.20	-1.68	-7.83	-2.44	-1.61	-7.86	-2.26	-2.17	-9.97	-1.93	-1.68	-7.80	-2.16	-1.27	-5.68
SBTD	14.98	12.16	16.75	14.82	12.07	16.48	15.70	12.79	18.36	15.14	12.25	16.62	14.27	11.53	15.54
R	0.75	0.81	0.65	0.75	0.81	0.66	0.73	0.78	0.59	0.74	0.80	0.66	0.77	0.83	0.70

6.2-μm	All			Spring			Summer			Autumn			Winter		
	CRA	ERA5	MERRA-2	CRA	ERA5	MERRA-2	CRA	ERA5	MERRA-2	CRA	ERA5	MERRA-2	CRA	ERA5	MERRA-2
MBTD	-0.78	0.78	-0.92	-0.83	0.75	-1.00	-0.85	0.73	-1.37	-0.70	0.82	-0.86	-0.73	0.84	-0.45
SBTD	4.43	3.78	5.05	4.36	3.68	4.94	4.53	3.96	5.54	4.41	3.80	4.98	4.40	3.67	4.75
R	0.87	0.90	0.82	0.87	0.90	0.82	0.87	0.89	0.79	0.87	0.90	0.83	0.88	0.91	0.86

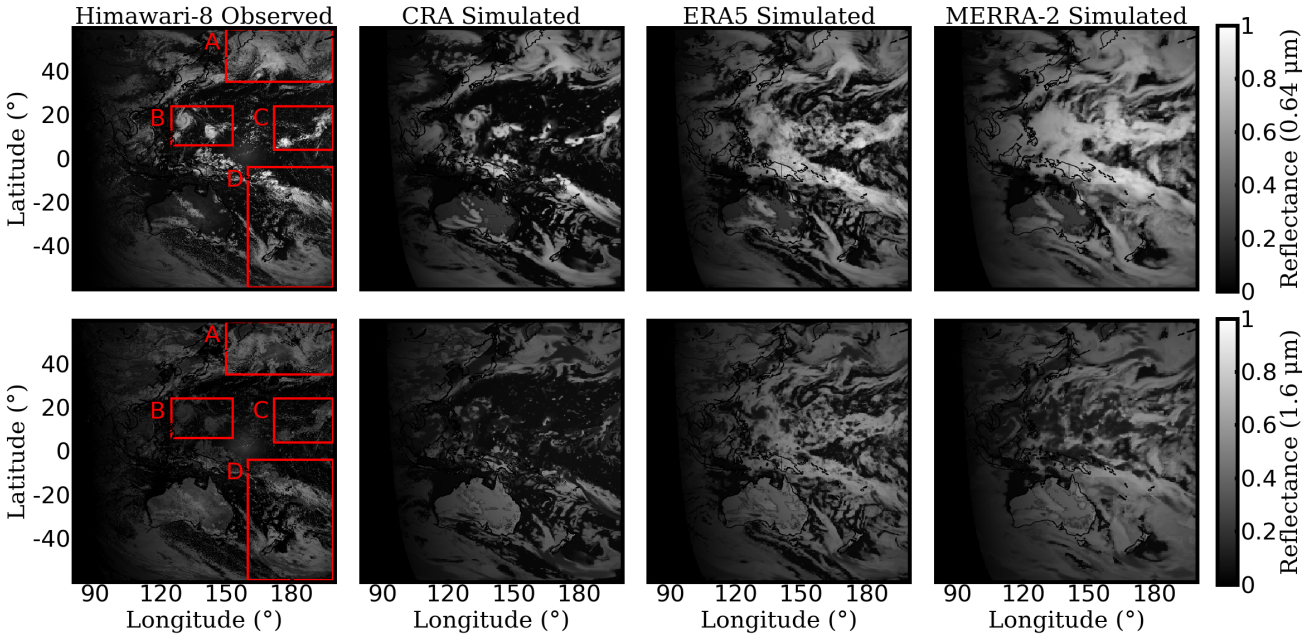

Figure 1. Observed and simulated reflectance in the 0.64-μm (top) and 1.6-μm (bottom) channels. The results are taken at 00:00 (UTC) on 12 September 2016.

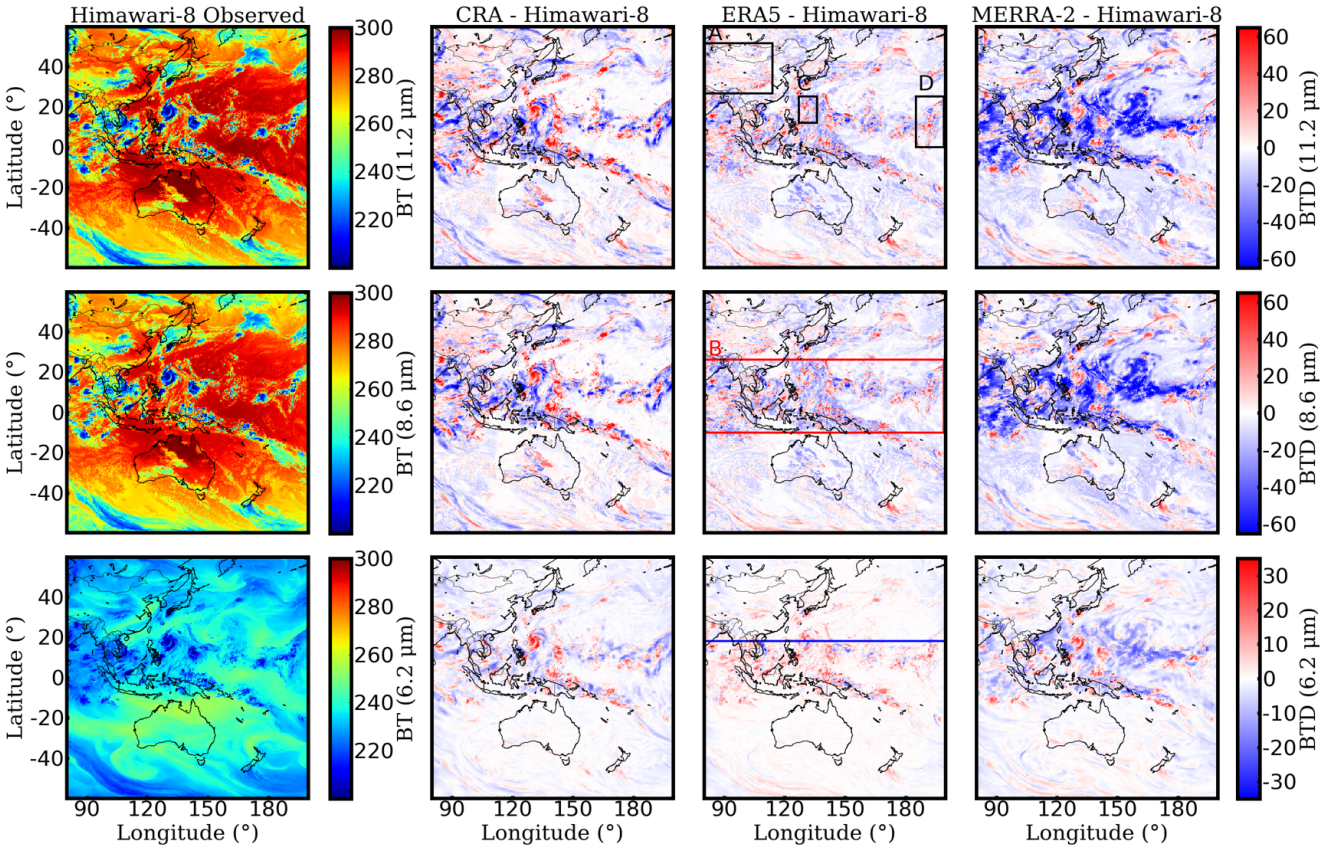

Figure 2. Observed results and the brightness temperature differences between the observations and simulations in the 11.2-μm (top), 8.6-μm (middle), and 6.2-μm (bottom) channels. The results are taken at the same time as that in Figure 1.

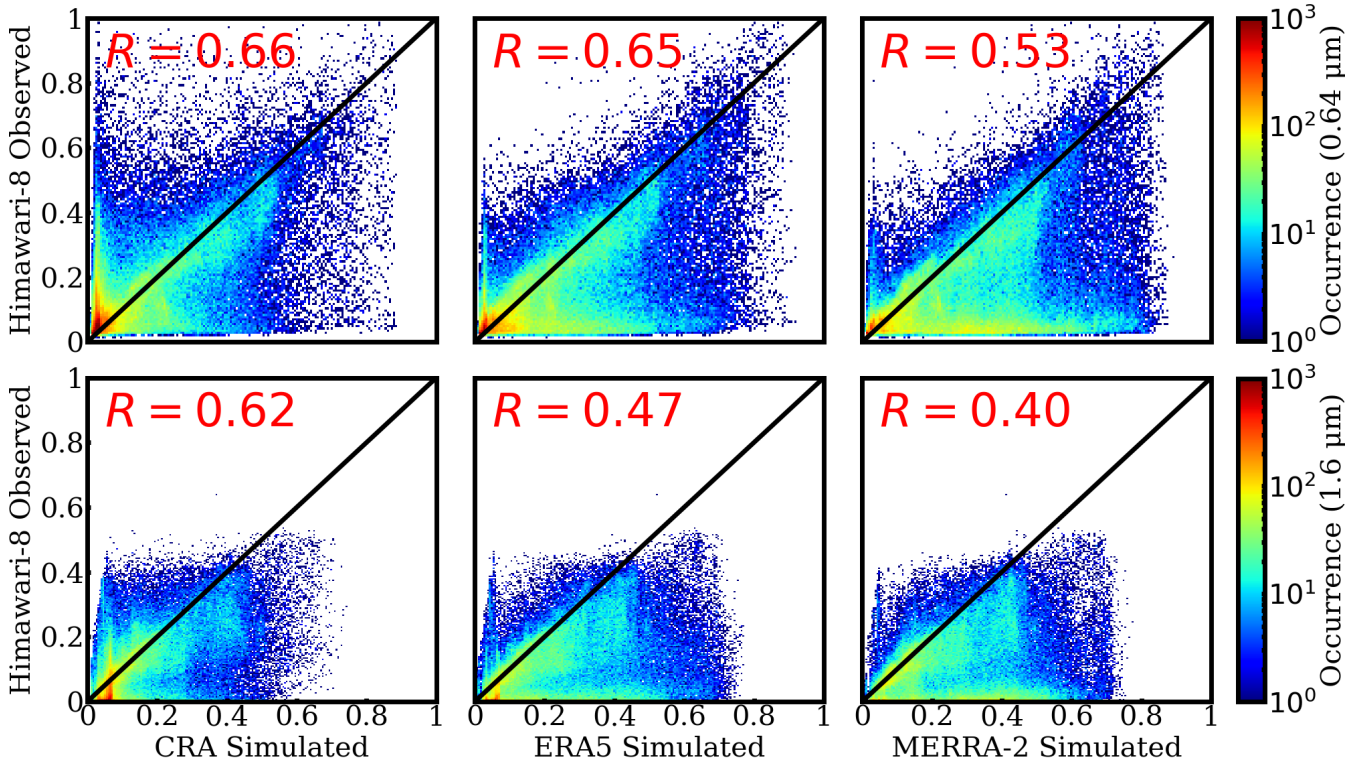

Figure 3. Pixel-to-pixel comparisons between the observed and simulated reflectance in the 0.64-μm (top) and 1.6-μm (bottom) channels. The histograms illustrate the occurrences of reflectance, and the results are taken at the same time as that in Figure 1.

630

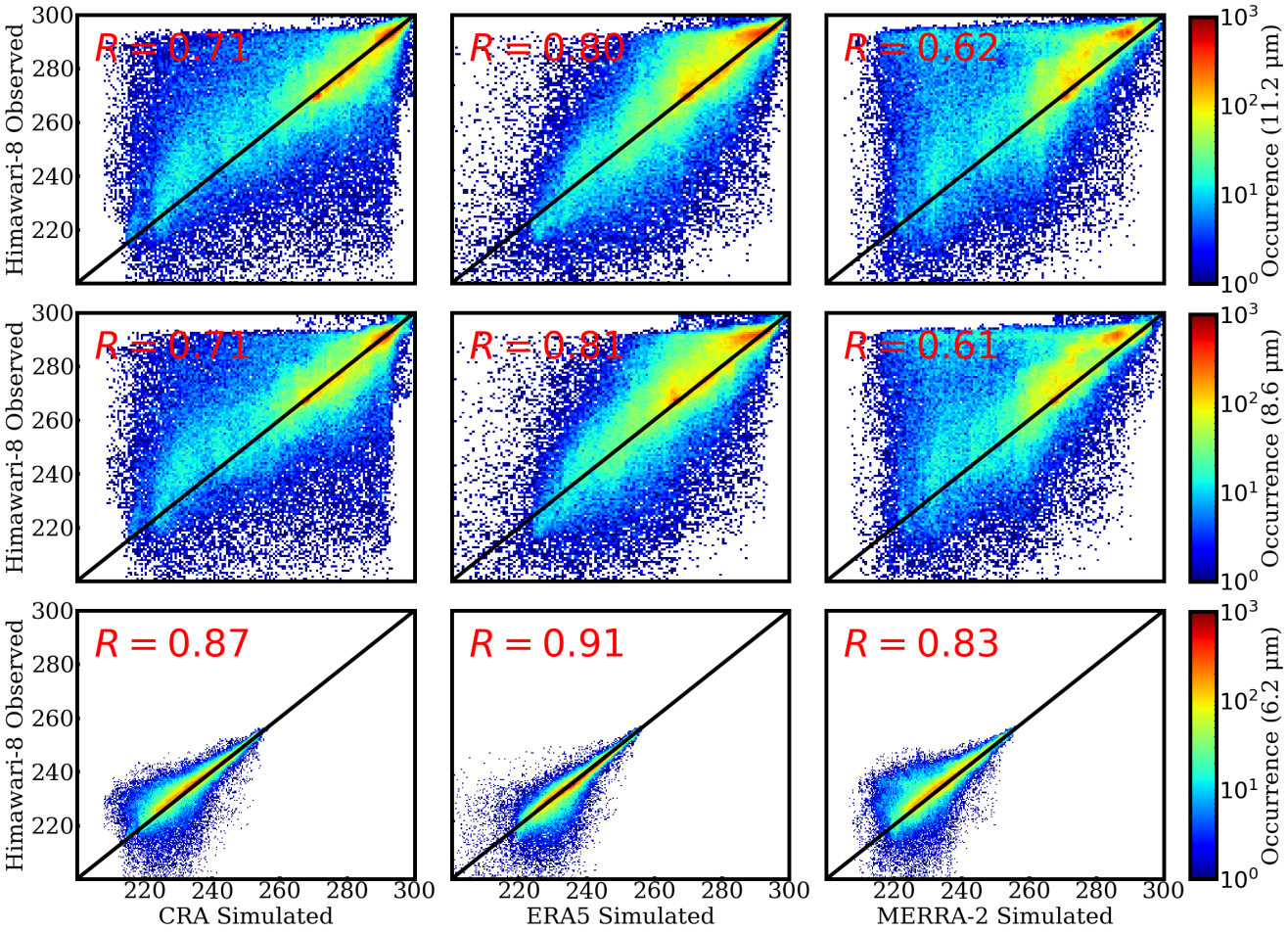

Figure 4. Same as the results in Figure 3, but for the infrared channels.

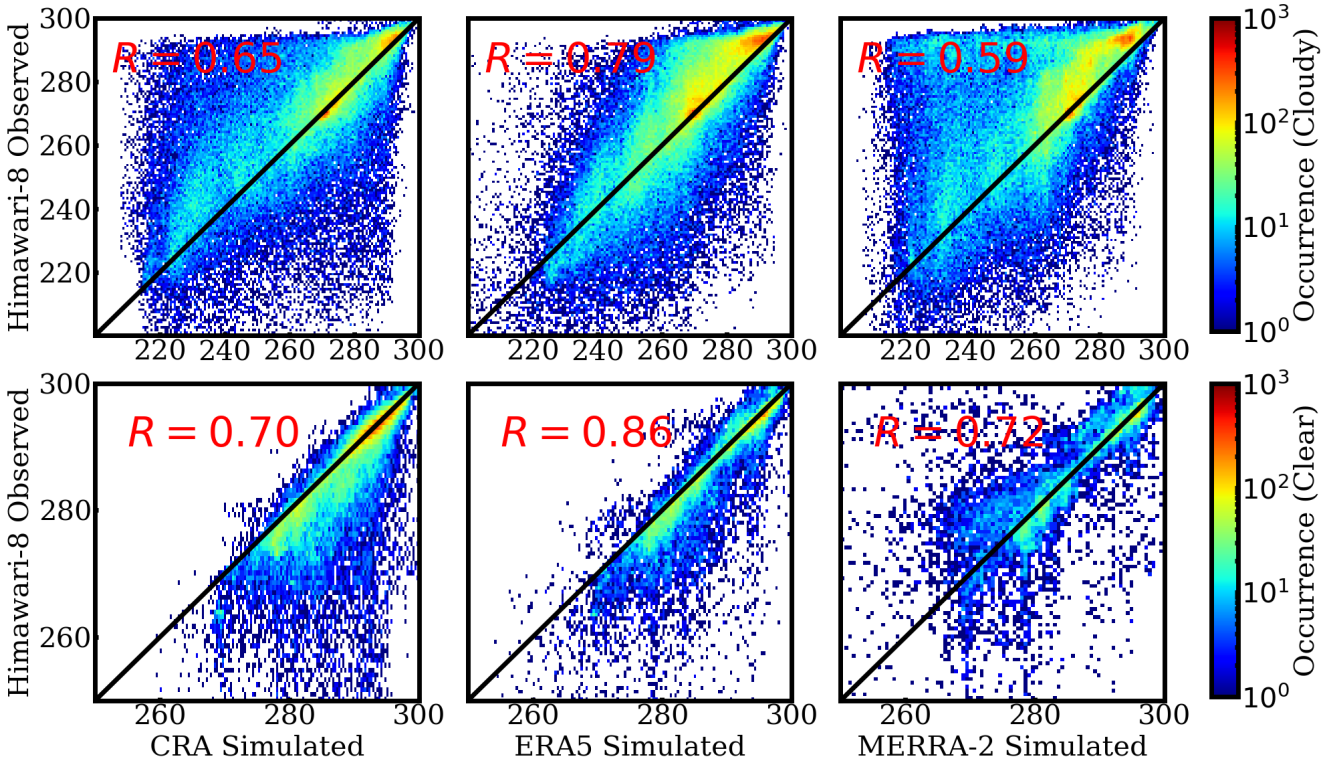

635 **Figure 5.** Comparisons between the observed and simulated BTs in the 11.2-μm channel with pixels for cloudy (top) and clear-sky (bottom). The results are taken at the same time as that in Figure 4.

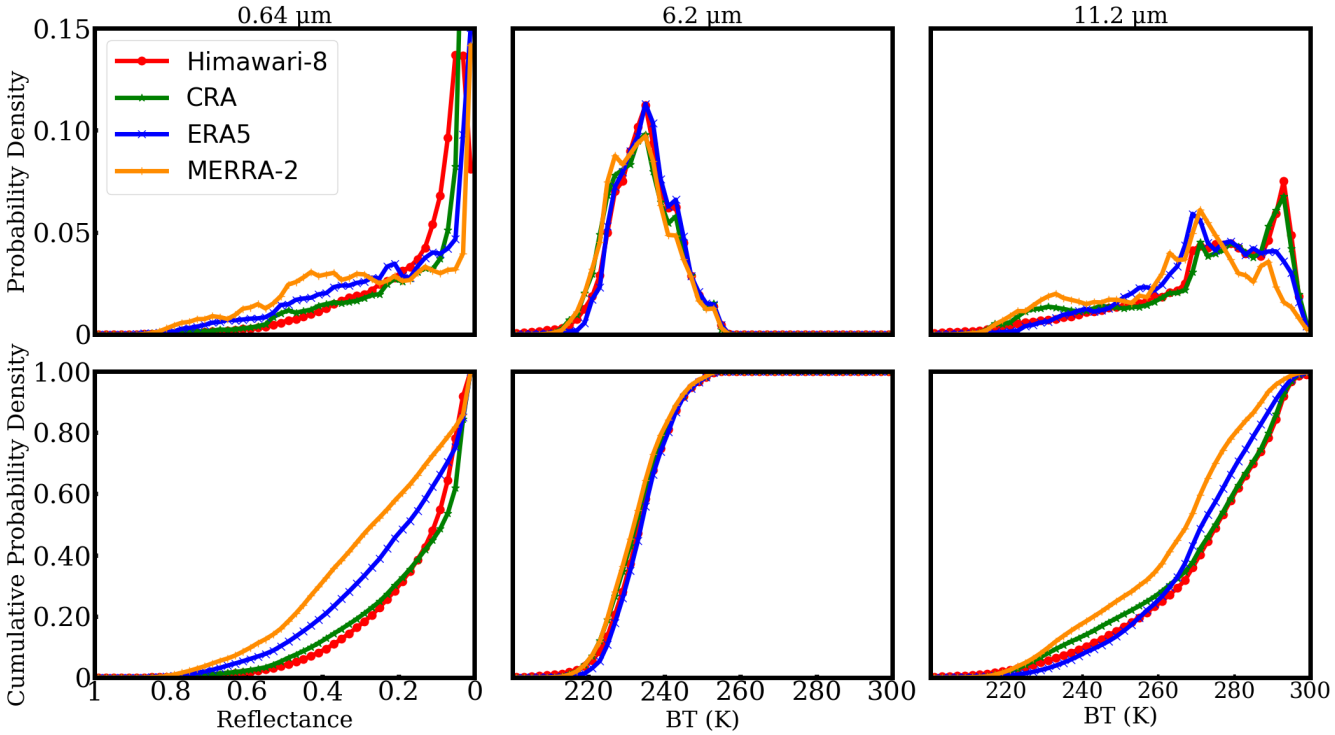

Figure 6. Probability and cumulative probability density for the observed and simulated reflectances in the 0.64-µm (left) channel and the BTs in the 6.2- (middle) and 11.2-µm (right) channels.

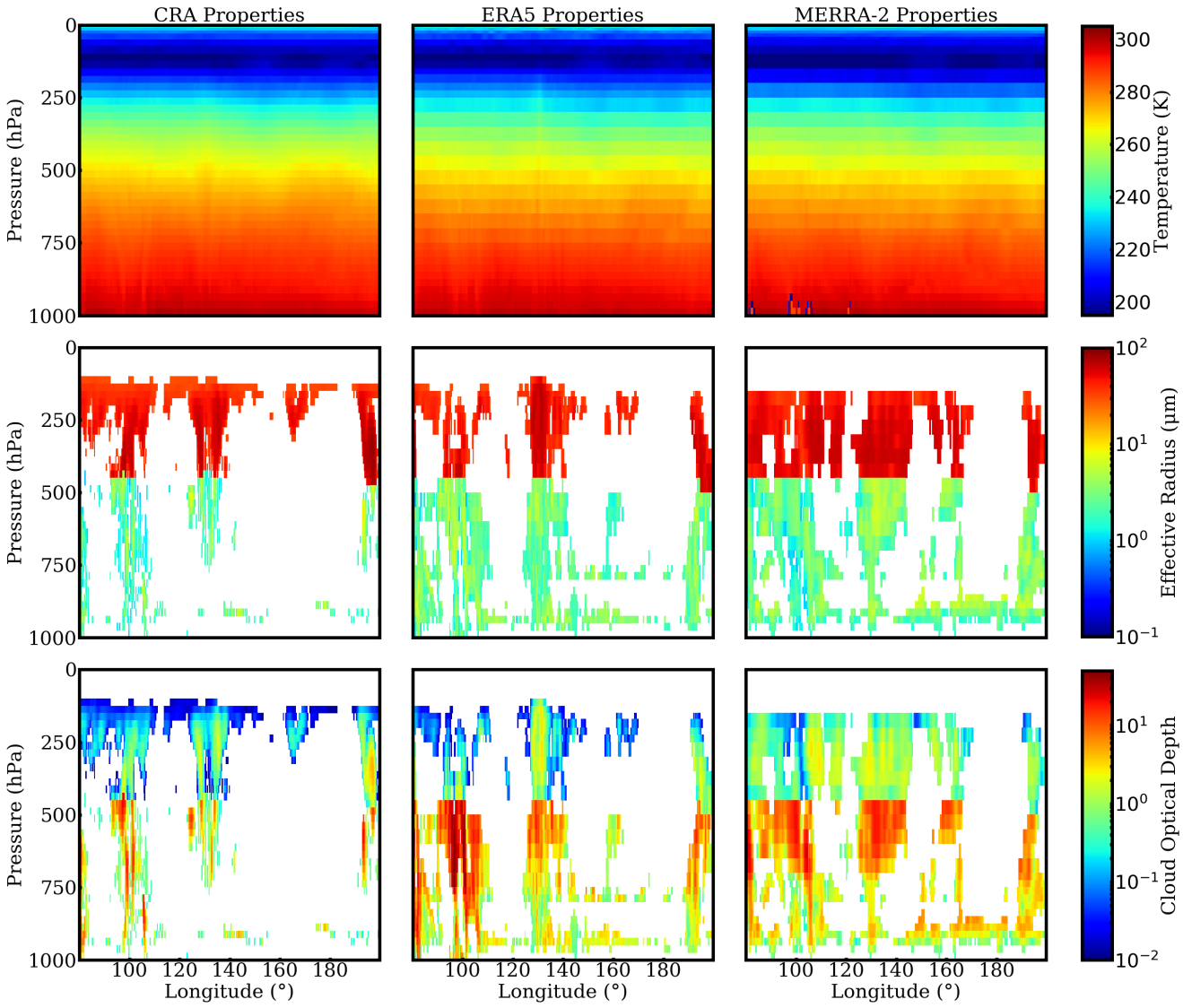

Figure 7. Comparison of the profiles of the temperature, cloud effective radius and optical depth in the CRA (left), ERA5 (middle), and MERRA-2 (right) reanalysis datasets. The profiles are for the track marked by blue solid lines in Figure 2.

645

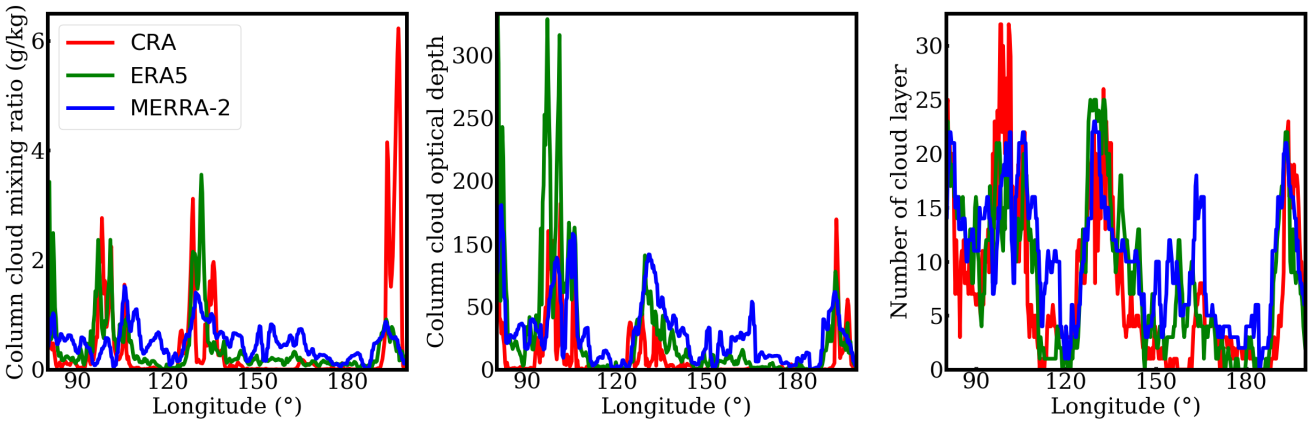

Figure 8. Column cloud mixing ratio (left), cloud optical depth (middle), and number of cloud layer (right) in each column. The results are from Figure 2 marked by blue solid lines.

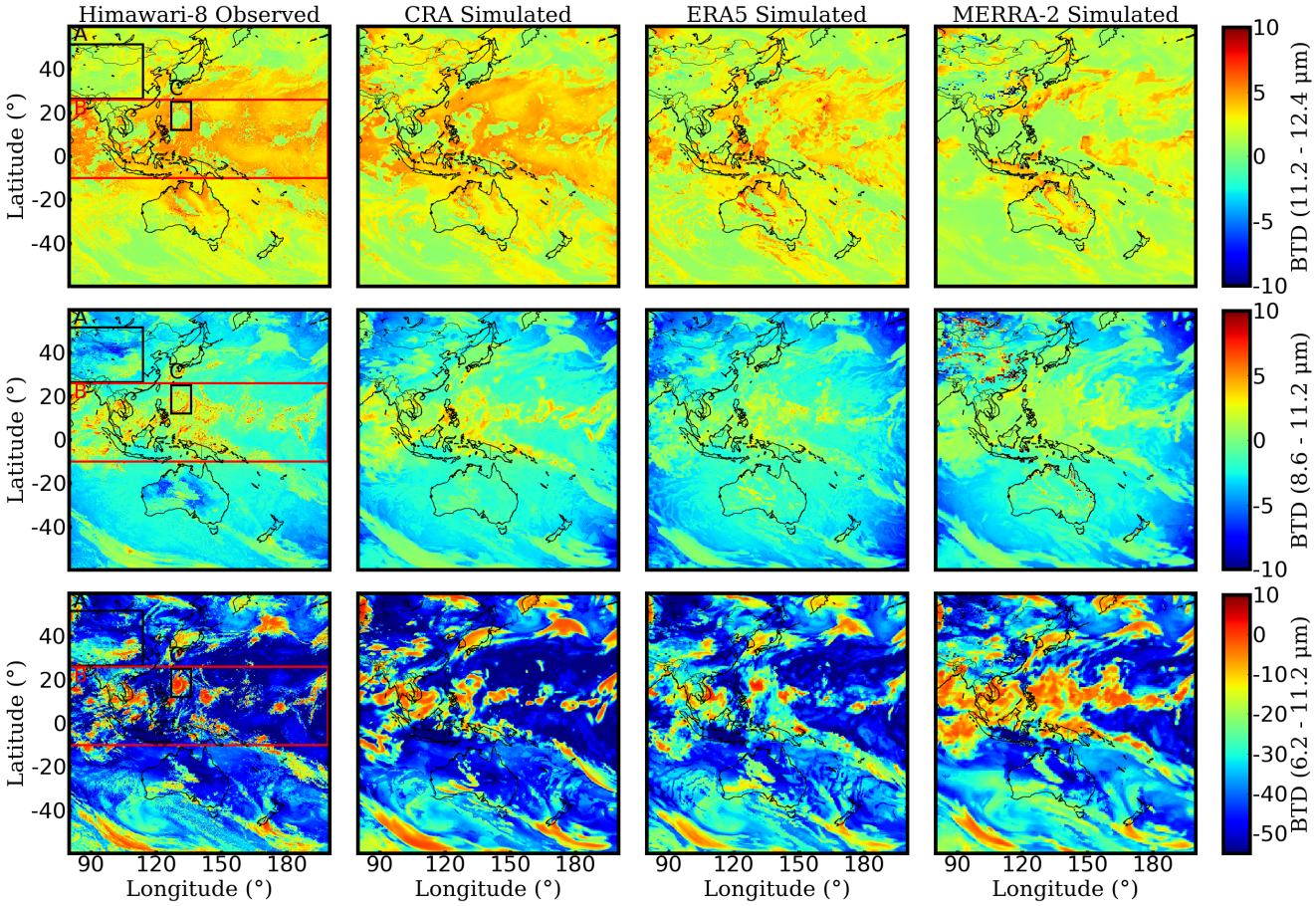

650

Figure 9. Observed and simulated brightness temperature differences of 11.2–12.4-μm (top), 8.6–11.2-μm (middle), and 6.2–11.2-μm (bottom). The results are taken at the same time as that in Figure 1.

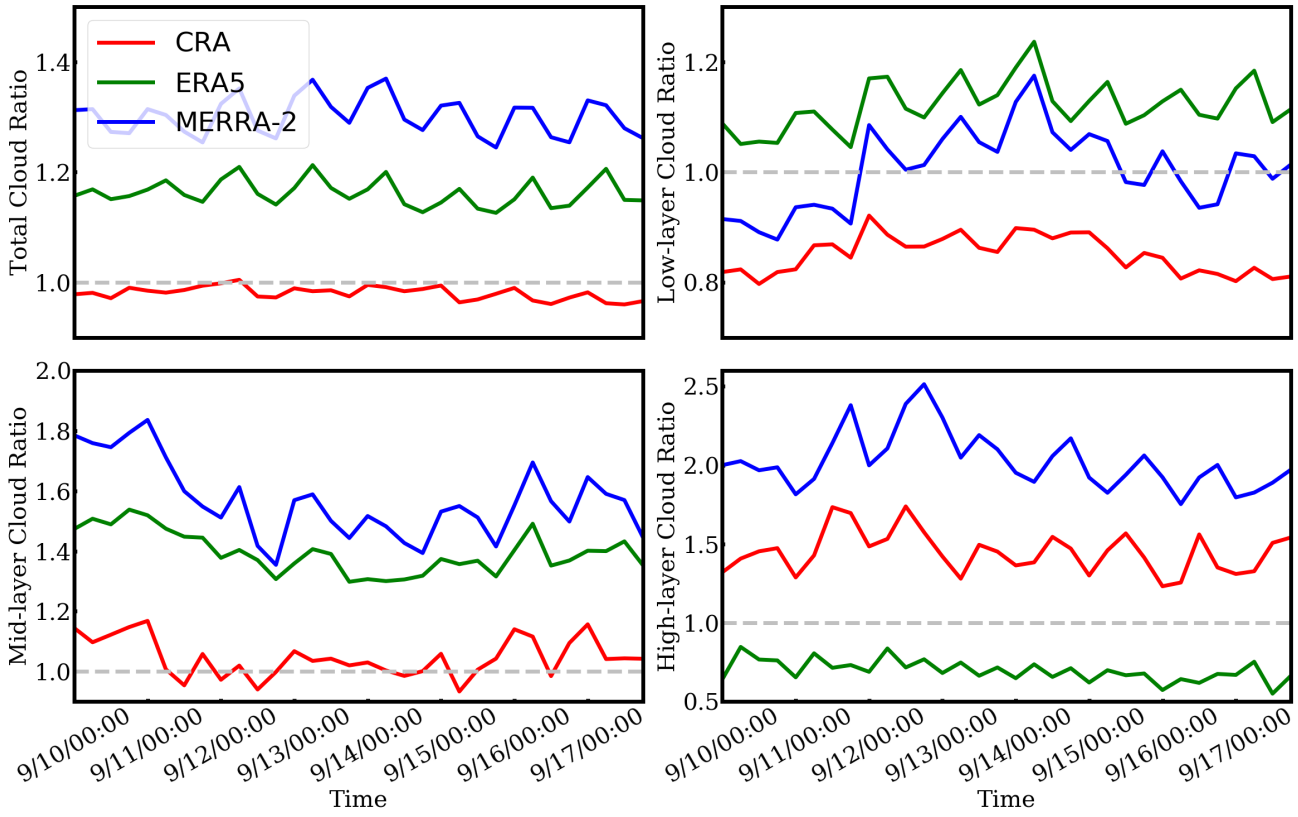

655 **Figure 10.** Temporal variation of the ratios (simulation-to-observation) for different layer clouds. The classification of clouds is based on the BTDs of 6.2-μm - 11.2-μm.

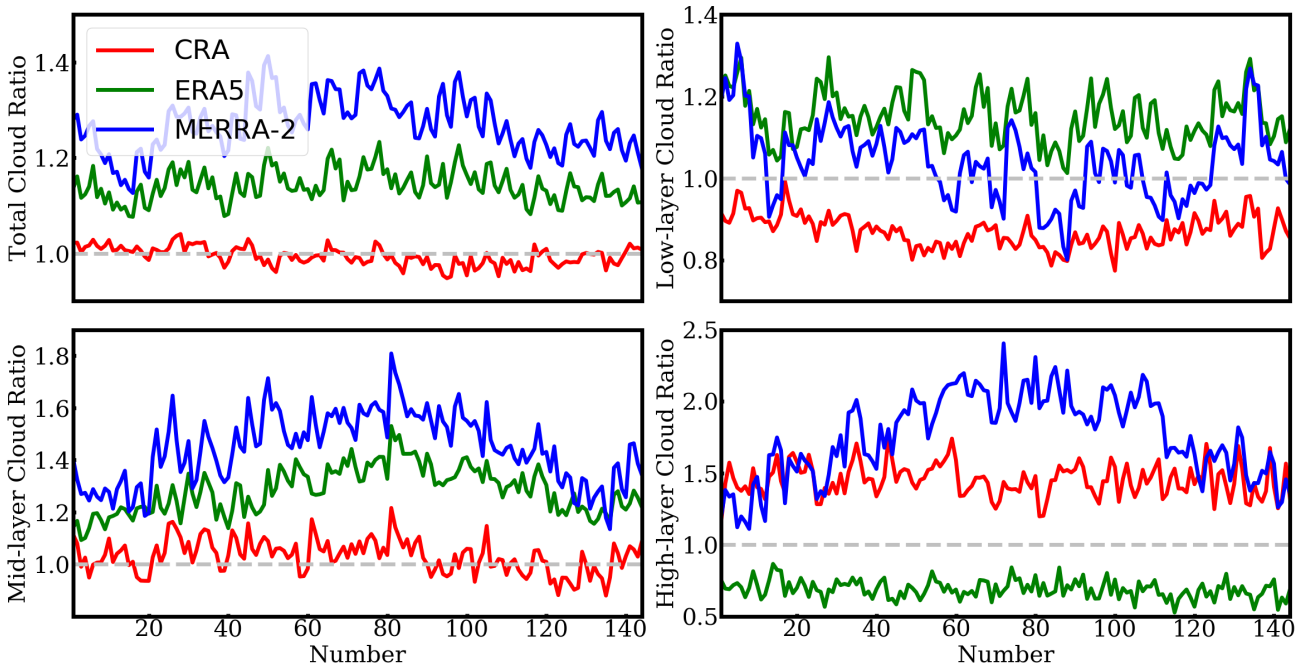

Figure 11. Same as Figure 10, but for the results from 144 realizations spanning over 2016.

660

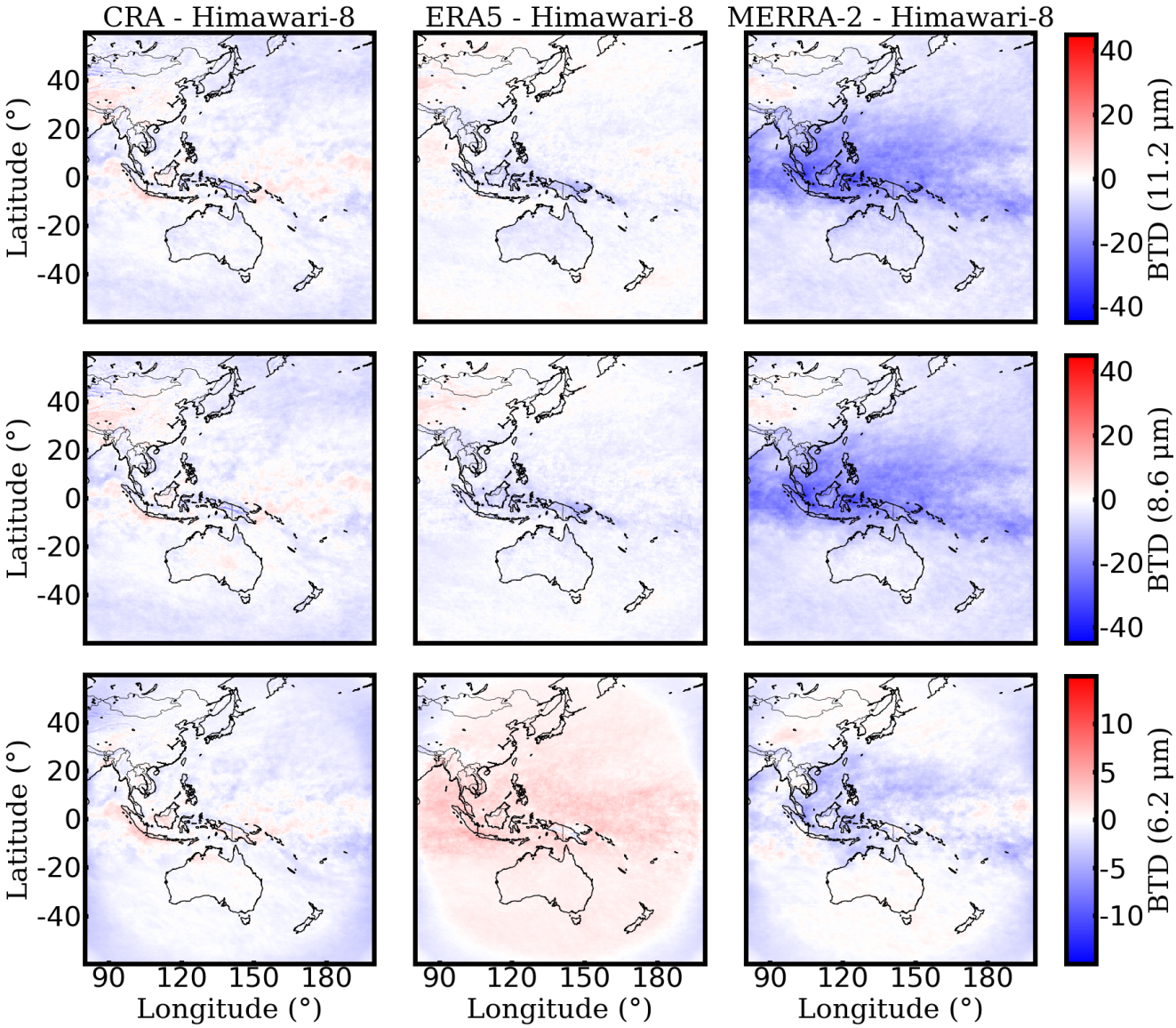

Figure 12. Average result of brightness temperature differences between the observations and simulations in the 11.2-μm (top), 8.6-μm (middle), and 6.2-μm (bottom) channels. The observations and simulations are from the 144 realizations spanning over 2016.

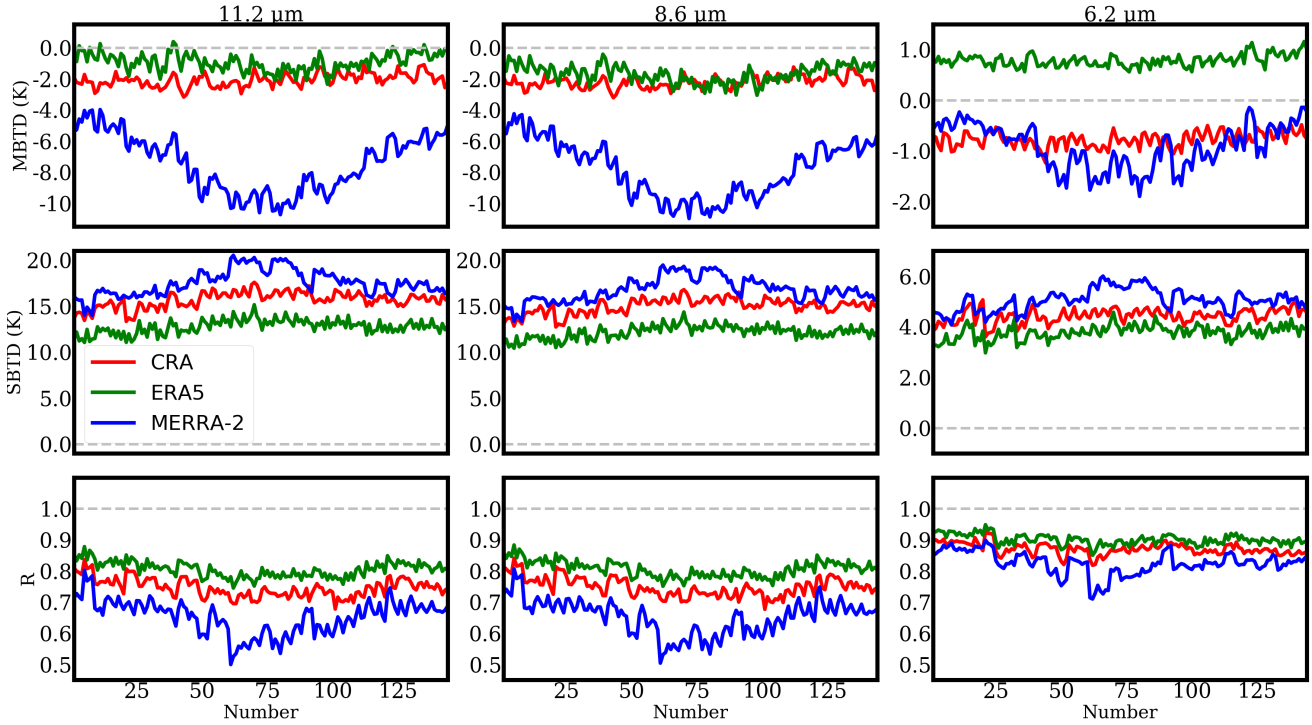

Figure 13. Temporal variation of three statistical parameters: the mean BTDs (MBTD), standard deviations of BTDs (SBTD), and correlation coefficient (R) between the observation and simulation. The results are from 144 realizations spanning over 2016.